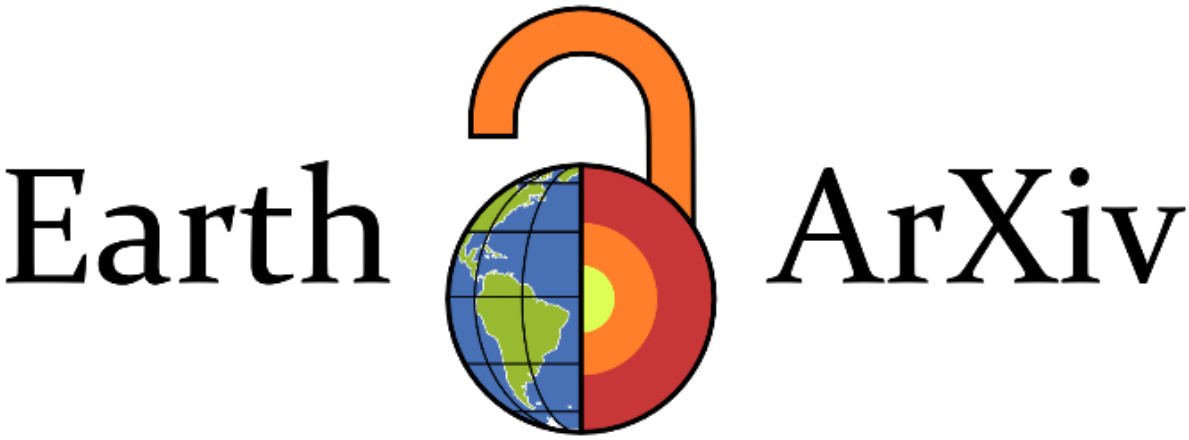

Regionally representative observations reveal coupled influence of meteorology and surface exchange on atmospheric mercury variability

Eric M. Roy[1,2], David A. Gay[3], Noelle E. Selin[1,2,4]*

[1]Department of Earth, Atmospheric, and Planetary Sciences, Massachusetts Institute of Technology, Cambridge, MA 02139, USA

[2]Center for Sustainability Science and Strategy, Massachusetts Institute of Technology, Cambridge, MA 02139, USA

[3]National Atmospheric Deposition Program, Wisconsin State Laboratory of Hygiene, University of Wisconsin Madison, Madison, WI 53706, USA

[4]Institute for Data, Systems, and Society, Massachusetts Institute of Technology, Cambridge, MA 02139, USA

KEYWORDS: Mercury, Gaseous Elemental Mercury, Chemical Transport Modeling, Box modeling, Diel variability, Atmospheric rectifier effect

ABSTRACT: The environmental fate of mercury (Hg) is determined by its atmospheric processing, yet the relative role of surface fluxes, chemistry, and transport on atmospheric loadings remains poorly understood. We use multiyear gaseous elemental Hg (Hg^0) concentration measurements at two rural sites and two urban sites in the northeastern US coordinated by the

National Atmospheric Deposition Program (NADP) together with models to identify drivers of diel variability. We observe that Hg^0 concentrations have similar magnitude and variability between measurement sites within urban or rural regions, with highest concentrations in the urban region. Concentrations within the rural and urban regions tend to converge at midday, reaching a maximum at rural sites and a minimum at urban sites, particularly in summer. Using a boundary layer box model and the GEOS-Chem chemical transport model, we show that this midday convergence is driven by the combined influence of regional surface fluxes and the entrainment of free tropospheric air, rather than in-situ chemical fluxes. Our results demonstrate that diel Hg^0 concentration variability can serve as a constraint on free tropospheric loadings of Hg^0 and can help identify biases in regional and global atmospheric budgets of Hg.

1 Introduction

Mercury (Hg) is a globally distributed neurotoxic pollutant which is subject to complex atmospheric processing that determines its deposition to vulnerable ecosystems[1–3]. Historical and ongoing anthropogenic activities have introduced significant quantities of Hg to the environment over the last four millennia, leading to an eightfold increase in its atmospheric burden[4,5]. The rate at which Hg is removed from the atmosphere is largely determined by its chemical speciation, which includes gaseous elemental Hg (Hg^0, >90% of tropospheric burden) along with gaseous and particulate-bound oxidized Hg (Hg^{II}, <10% of tropospheric burden)[6–8]. Hg^0 has a long atmospheric lifetime and is removed by vegetative uptake or oxidation to Hg^{II} [8,9], while Hg^{II} is highly soluble and readily removed from the atmosphere via wet or dry deposition[10,11], or may be converted to Hg^0 via photoreduction[8,12]. In addition to direct anthropogenic and geogenic Hg emissions, previously deposited mercury can be reemitted from surfaces, leading to its continual recycling in

41 the environment[5]. Therefore, the atmospheric concentration of Hg at a given location will be
42 determined by the combined influence of emission, deposition, chemistry, and atmospheric
43 transport processes that act on local to global scales.

44 The diel variation of Hg^0 at urban and rural measurement sites has been explained by several
45 different mechanisms in existing literature, including chemical, surface exchange, and
46 meteorological forcings. Long term measurements made possible by national and international
47 monitoring networks have shown that average Hg^0 concentrations in urban regions are often higher
48 than rural regions, consistent with the expected impact of modern and historical anthropogenic
49 emissions[13,14]. These observations have also shown that diel variations of atmospheric Hg^0 in urban
50 and rural regions are effectively out of phase with one another, with Hg^0 lowest at midday at urban
51 sites and highest at midday at rural sites. Early studies observed that this daytime decline of Hg^0
52 at urban sites coincided with a daytime maximum in Hg^{II} and argued that this variability could be
53 explained by O_3-mediated oxidation in polluted regions[15,16]. However, a recent study using robust
54 Hg^{II} measurements found that these elevated Hg^{II} concentrations were likely driven by free
55 tropospheric input rather than in-situ oxidation[17]. In contrast to urban areas, Hg^0 concentrations in
56 vegetated rural areas are typically highest at midday and lowest before dawn[18–20]. This pattern is
57 counterintuitive given the growing consensus that vegetation acts as a net sink of Hg^0, where
58 photosynthetically-driven uptake should be strongest at midday[21,22]. Studies have argued that
59 daytime Hg^0 concentration peaks may be driven by the reemission of Hg from short-term
60 reservoirs, including previously deposited Hg^{II} on cuticular surfaces[23], or the uptake and
61 subsequent reemission of Hg^0 by dew formation and evaportation[23,24]. However, hypothesized
62 reemission pathways were not observed in ecosystem-scale flux measurements carried out at two
63 rural sites in the northeastern US, instead showing that underlying forests act as a strong sink

during daylight hours and a slight sink overnight during vegetatively active seasons[25]. A recent controlled experiment found that tropical vegetation also acted as a strong sink during daylight hours and a weak sink overnight, though mechanisms for this variability remain unclear[26].

Several studies have identified that the diel behavior of Hg in urban and rural areas may be explained by atmospheric boundary layer variability and mixing. Nair et al.[19] compared Hg^0 concentrations at urban, rural, and suburban sites in the southeastern US and used correlation-based arguments to conclude that boundary layer entrainment was a key driver of differences in diurnal variations across sites, rather than chemical fluxes. More recently, Roy et al.[20] compared the seasonal and diel variation of Hg^0 concentrations and Hg^0 ecosystem uptake fluxes at two rural forests in the northeastern US, finding that concentrations are highest when uptake fluxes are strongest, and argued that the out-of-phase behavior could be explained by the combined influence of variations in surface fluxes and the downwelling of free tropospheric air. Furthermore, Denzler et al.[27] showed that a simple boundary layer box model could be used to quantify emissions in an urban area under specific meteorological conditions, demonstrating the important impact of meteorology on concentration variability. However, the relative contribution of chemistry, surface fluxes, and transport fluxes (i.e., boundary layer entrainment, horizontal advection) to diel variability has not been extensively studied in existing chemical transport models (CTMs).

Here, we investigate the drivers of spatial and diel variation of Hg^0 concentrations at four measurement sites (two urban, two rural) in the northeastern US coordinated by the National Atmospheric Deposition Program (NADP) Atmospheric Mercury Network (AMNet). We first characterize the diel variation across the sites in both June and December, representing summer and winter months, respectively. We then use a boundary layer box model adapted from Denzler et al.[27] that is driven by observationally derived meteorology to calculate the regional surface

fluxes that reproduce observed Hg^0 concentrations at rural and urban sites for a given set of boundary conditions. Finally, we compare the range of calculated regional surface fluxes to those used by the GEOS-Chem CTM and explore the relative sensitivity of modeled concentration variability to regional surface and transport fluxes.

2. Methods

We first describe the four measurement sites evaluated in this study (section 2.1), and then describe our implementation of the GEOS-Chem CTM in this paper (section 2.2). Finally, we discuss the boundary layer box model that we use to efficiently investigate the drivers of concentration variability in the rural and urban regions represented by our observations (section 2.3).

2.1 Measurement Sites

Formally launched in 2009, NADP AMNet was designed to provide concentration measurements of Hg^0 and Hg^{II} (gaseous and particulate-bound) that could be used, in part, to infer the dry deposition of Hg to North America[13]. We use Hg^0 measurements from four sites in the northeastern US that were active for at least one year between 2011 and 2019 (inclusive) and exclude analysis of Hg^{II} based on its secondary contribution to atmospheric Hg burdens, along with the growing consensus that Hg^{II} measurement techniques used by current networks exhibit a significant and spatially variable low bias[28]. We select the New Brunswick, NJ (NJ30) and The Bronx, NY (NY06) sites to represent urban conditions, located approximately 45 km SW and 15 km NE of midtown Manhattan, respectively. Measurements taken at the Huntington Wildlife Forest, NY (NY20) and on the slopes of Mt. Mansfield in Underhill, VT (VT99) are located approximately 400 km N of Manhattan and represent rural conditions (Figure 1). These sites were selected, as they exhibit seasonal and diel concentration variations that are consistent with previous

regional analyses. We formally evaluate the consistency of concurrent hourly observations at different sites in Supplemental section S1.3 to support our interpretation of these sites as regionally representative. We find higher positive correlations of sites within a given region and values near zero between sites in different region types in June. Meanwhile, we find weak positive correlations among nearly all sites in December, consistent with the weak variability measured at all four sites in this dormant season, along with the increased influence of synoptic scale forcing during midlatitude winter. While observations are also available for the Elizabeth, NJ site (NJ54) since 2015, we exclude this site from our analysis due to extremely high average concentrations, which suggest that this site is influenced by local pollution sources (Figure S1). One potential source is the Phillips 66 oil refinery that is located approximately 1 km WSW of NJ54, which is listed as the 7th largest Hg source in New Jersey by the 2020 EPA National Emission Inventory[29], among a number of other local sources that were identified by Aucott et al.[30]. A summary of site characteristics for the NADP sites we consider is included in Table S1.

Hourly Hg^0 concentration measurements were downloaded from the AMNet website and used without further outlier filtering, as NADP conducts their own quality control that is described on their website (http://nadp.slh.wisc.edu/siteops/#amnet). Diel cycles of Hg^0 at each site were determined by calculating the average concentration for each hour of each day in the month of interest for all available years, and missing measurements were ignored by our averaging technique. We primarily analyze Hg^0 concentrations from June and December, which we show are representative of the typical diel variation at each site for summer and winter, respectively (Figure S4).

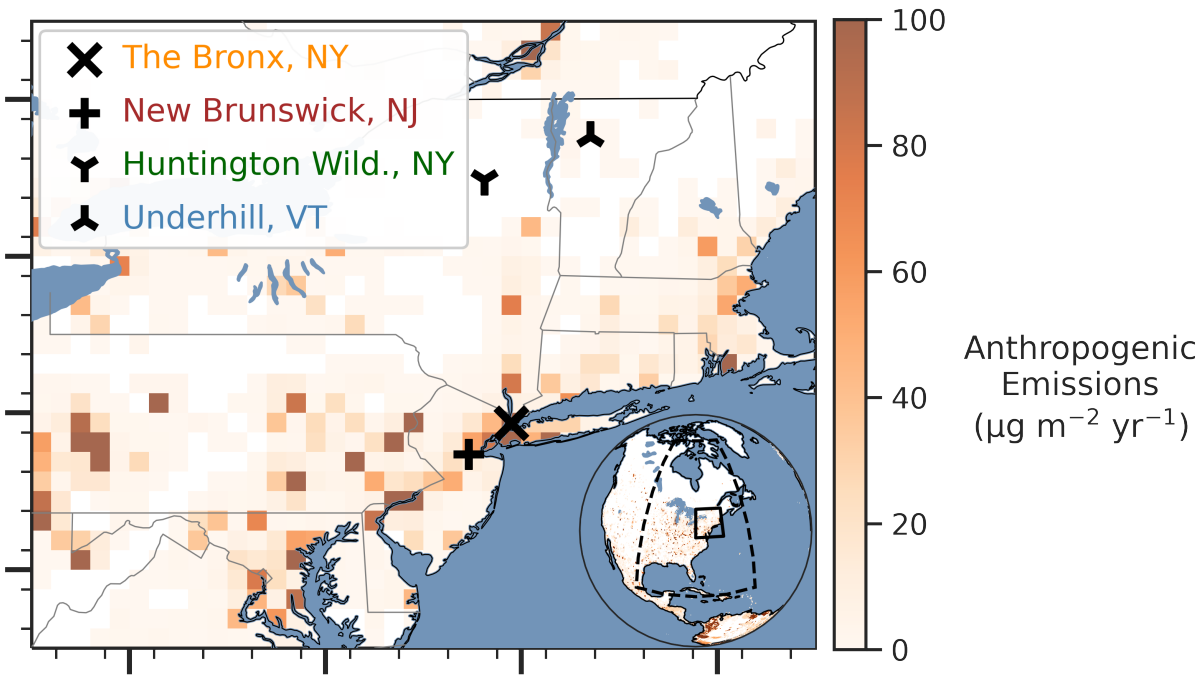

Figure 1. Location of rural (Underhill, VT and Huntington, NY) and urban (The Bronx, NY and New Brunswick, NJ) NADP sites explored in this study. Shading refers to the annual anthropogenic emissions predicted by the GMA emission inventory[31]. Major ticks represent the bounds of GEOS-Chem 2° latitude by 2.5° longitude grid boxes and minor ticks represent bounds of GEOS-Chem 0.5° latitude by 0.625° longitude grid boxes. Inset: The solid box represents the northeastern US domain, while the dashed box represents the entire domain covered by nested GEOS-Chem simulations.

2.2 GEOS-Chem

We simulate the atmospheric concentration of Hg^0 using the GEOS-Chem CTM (v14.1) to investigate its treatment of spatial and temporal variability at regional scales. This version of the model leverages the three-step oxidation mechanism described by Shah et al.[8] and the updated dry deposition scheme introduced by Feinberg et al.[6]. We drive the model with 2015 anthropogenic emissions produced for the 2018 Global Mercury Assessment[31] (GMA, Figure 1). Like other

currently published inventories, GMA provides annually averaged emission rates for 2015 and does not provide monthly or hourly disaggregation. Our use of constant fluxes is supported by a recent study of $PM_{2.5}$ diel variability in the GEOS-Chem model which found that upgrading to an hourly emission inventory had a secondary impact on simulated diel concentration variability in urban areas of the United States[32].

Each simulation is run for 2018 and 2019, where 2018 data is discarded as model initialization. The model is run at its standard spatial resolution (2° latitude by 2.5° longitude with 47 vertical layers), which we refer to as the STND simulation. We then use this simulation to produce boundary conditions for a nested simulation (0.5° latitude by 0.625° longitude with 47 vertical layers) spanning eastern North America (20°-70° N, 50°-100° W, dashed box in Figure 1), allowing us to evaluate the impact of horizontal resolution on simulated Hg^0 concentrations, which we refer to as NEST.

We also conduct nine sensitivity simulations based on NEST to evaluate the impact of enhancements to regional emissions and free tropospheric loadings on surface concentrations at these sites (Table S4). We first assess the impact of emissions with three simulations where GMA anthropogenic emissions are scaled by factors of 3, 7 and 10 within the domain bounded by Figure 1 (70°W-80°W, 40°N-50°N), referred to as ANT3, ANT7, and ANT10, respectively. We specifically select enhancements of 3 and 7 based on the recommendations of an existing study of the Greater Boston area[33], which argued that bulk emissions likely needed to be enhanced, potentially driven by underestimated waste emissions and secondary emissions. Therefore, we consider these anthropogenic emission perturbation simulations to represent the net impact of primary emissions, as well as secondary emissions that would by highest near densely populated, polluted areas. We run an additional three sensitivity simulations where emissions throughout the

nested domain are scaled by 3, 7, and 10 to evaluate the impact of enhancing emissions across most of eastern North America, referred to as ANT3-ENA, ANT7-ENA, and ANT10-ENA, respectively. Two other sensitivity simulations use standard GMA anthropogenic emissions but uniformly increase free tropospheric Hg^0 concentrations throughout the nested domain to approximately 1.4 ng m^{-3} (CFTSCAL) and 1.8 ng m^{-3} (CFTSCALMAX), respectively, allowing us to assess the impact of free tropospheric loadings on surface concentrations. Our final sensitivity simulation (CFTSCAL-ANT7-ENA) includes the regional emission scaling of the ANT7-ENA simulation and the free tropospheric concentration enhancement of the CFTSCAL simulation to investigate how their simultaneous adjustment can impact Hg^0 variability.

2.3 Box model

We construct a simple boundary layer box model following the same motivations that underpin CTMs to efficiently explore the impact of key fluxes on the temporal variability of Hg^0. Discretized CTMs implicitly assume that spatial concentration gradients within a grid box are negligible (i.e., well-mixed). Here, we adapt a model originally presented by Denzler et al.[27] to simulate the temporal evolution of Hg^0 concentrations within the planetary boundary layer (PBL) ($\frac{dc_{pbl}}{dt}$, ng m^{-3} hr^{-1}) at rural and urban sites, where horizontal and vertical extents selected to satisfy the assumption of a well-mixed atmosphere, as shown in equation 1:

$$\frac{dc_{PBL}}{dt} = \frac{u(c_{UW} - c_{PBL}(t))}{x} + \frac{w_{PBL}(c_{FT} - c_{PBL}(t))}{z} + \frac{F}{z} + F_{chem} \quad (1)$$

In this equation, u is the horizontal wind magnitude within the PBL (m hr^{-1}), w_{PBL} is the growth rate of the PBL (m hr^{-1}), x is the horizontal extent of the box (m), z is the vertical extent of the box (PBL height, or PBLH, with units m), F is the surface flux within the box (ng m^{-2} hr^{-1}), F_{chem} is the net production of Hg^0 within the box (ng m^{-3} hr^{-1}), and C_{UW} and C_{FT} represent the upwind and free tropospheric concentrations of Hg^0, respectively. From left to right, the four terms of equation 1

represent the horizontal advection flux, entrainment flux, the net surface exchange flux, and net chemical production. We neglect F_{chem} in our box model and test this assumption in section 3.1 by comparing its magnitude in the GEOS-Chem CTM within the PBL to net surface fluxes. Further evaluation of this box model and its sensitivity to assumptions is included in supplemental section S2.

We configure the box model to capture the average regional variability given an average set of meteorological conditions and fluxes, similar to the typical configuration of global CTMs. We define x to be 100 km, which is approximately equivalent to a 0.9° latitude by 0.9° longitude grid in this region. We justify the spatial extent of our box model with the coherence of measurements within urban or rural sites, supporting the assumption that our box model represents a well-mixed region (see section 3.1). We then define u, z, and w_{pbl} using a previously dataset that provides hourly vertical profiles of horizontal windspeeds and PBLH calculated using aircraft data available at 50 airports within the continental US between 2010 and 2020[34,35]. We use 2017 meteorological data rather than averaging PBL profiles interannually due to variations in the quantity and quality of aircraft-derived profiles. We evaluate the sensitivity of our findings to this simplification in supplemental section S2.5, to which we find a minimal impact on the key messages of this work.

Regionally representative meteorological conditions are defined as the average of profiles collected at Newark Liberty International Airport (Newark, NJ) and Bradley International Airport (near Hartford CT). We then select the month of interest and calculate the average PBLH and horizontal windspeed for each respective hour, resulting in a single 24 hour diurnal cycle that is repeated for each day of the month. Due to the limited amount of data that are used to calculate these cycles ($n \leq 31$ data points for each hour), we apply a centered rolling average with a five hour window to define the average boundary layer variation for this region (Figure S6), which we

find to be similar to the PBLH from the MERRA2 reanalysis product that drives GEOS-Chem (Figure S7). Using this smoothed profile, we calculate w_{PBL} as the hourly change in PBLH. The entrainment term is nonzero only when w_{PBL} is positive (i.e., dawn-midday)[27,36], as the communication of C_{PBL} and C_{FT} is mediated by convective thermals that overshoot the previous PBLH during periods of growth. Meanwhile, PBLH declines are caused by weakening convective thermals that do not reach the existing PBLH, meaning that mixing at the top of these plumes would occur on air that was already in the PBL. We follow a similar approach to calculate a smooth, daily repeating pattern for u which represents the average wind magnitude at each profile level that is below the PBLH (Figure S8).

We identify constant surface fluxes that minimize the difference between the boundary layer box model and the observed average Hg^0 concentration for the month and region of interest. We calibrate F to minimize the residual between the box model average Hg^0 concentration and the observed monthly average Hg^0 concentration for a given combination of C_{UW} and C_{FT}. This exercise is conducted for both June and December to isolate seasonal impacts. Since the average monthly concentrations are higher in urban regions than rural regions, the calibrated flux for each region will be different even if the same values of C_{UW} and C_{FT} are assumed. We assume that F does not vary in time based on previous studies that have shown that Hg^0 fluxes are generally unidirectional over day and night periods in rural areas[20,25], and has been previously utilized to estimate urban Hg emissions in Zurich[27]. This unidirectionality of diel surface fluxes means that applying an average flux value for each hour will not artificially bias the diurnal variations of concentrations, as would be the case for trace species that switch from sources to sinks over diel periods, like CO_2[37]. This is further justified in supplemental section S2.6, where we reevaluate this

optimization while allowing fluxes to vary diurnally, which does not notably change the average surface flux and leads to overfitting of the box model.

3. Results and discussion

We first compare measured concentrations at the four sites to simulations of the GEOS-Chem model and our boundary layer box model, and discuss the possible contribution of chemistry, local surface fluxes, and transport fluxes to observed Hg^0 concentrations and their variability (section 3.1). We then conduct a sensitivity analysis to identify the relative contribution of regional surface fluxes and transport fluxes on biases in the GEOS-Chem model (section 3.2). After diagnosing the sensitivity of diel concentration variability to enhancements of regional surface fluxes and transport fluxes in the rural and urban regions (section 3.3), we discuss implications for Hg modeling and monitoring efforts (section 3.4).

3.1 Measured and modeled Hg^0 concentrations

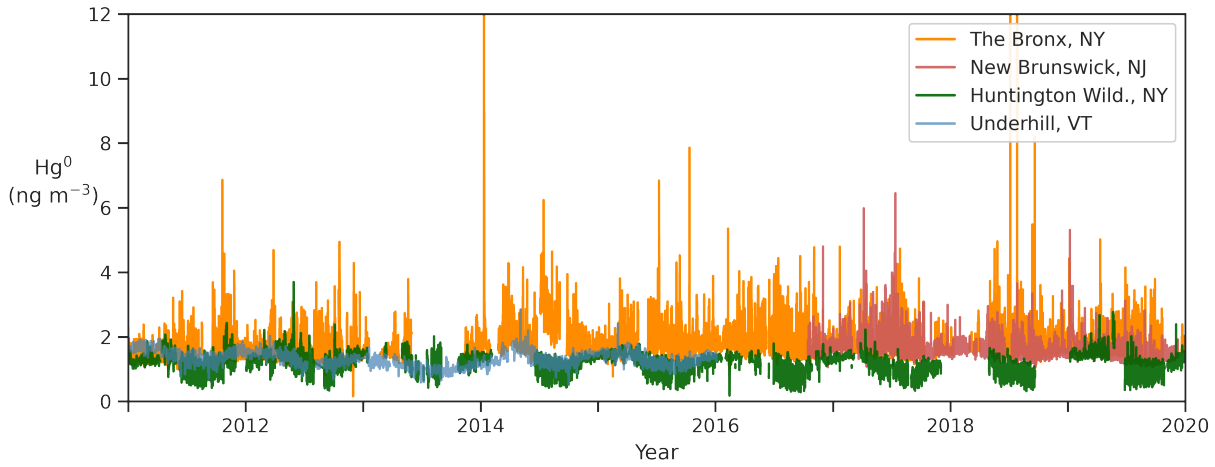

Figure 2. Hourly concentrations at The Bronx NY (orange), New Brunswick NJ (red), Huntington Wildlife NY (green), and Underhill VT (blue).

The magnitude and variability of hourly Hg^0 concentrations are largely consistent within urban or rural regions but differ notably across region types at the four NADP sites considered (Figure

2). Concentrations at urban sites are typically higher than rural sites, with the highest values observed at The Bronx and the lowest observed at Huntington. Concentrations at the rural sites exhibit expected northern hemispheric seasonality, where concentrations are highest in late winter and lowest in late summer, consistent with the previously identified vegetative control on Hg^0 concentrations[21–23]. Seasonality at urban sites is largely masked by strong summertime variability, with concentrations occasionally above 6 ng m^{-3} at both urban sites and as high as 20 ng m^{-3} at The Bronx, highlighting the occasional influence of local pollution sources. Concentrations at rural sites rarely exhibit discrete concentration peaks, but are most variable during summer months, when values consistently reach as low as 0.5 ng m^{-3} at Huntington. Interestingly, urban concentrations throughout the measurement period appear to reach a lower bound that is nearly equivalent to the upper bound of concentrations at rural sites. This convergence point exhibits the same previously noted seasonality, except for one three-month period in early 2019 where concentrations at Huntington exhibit unexpectedly high values.

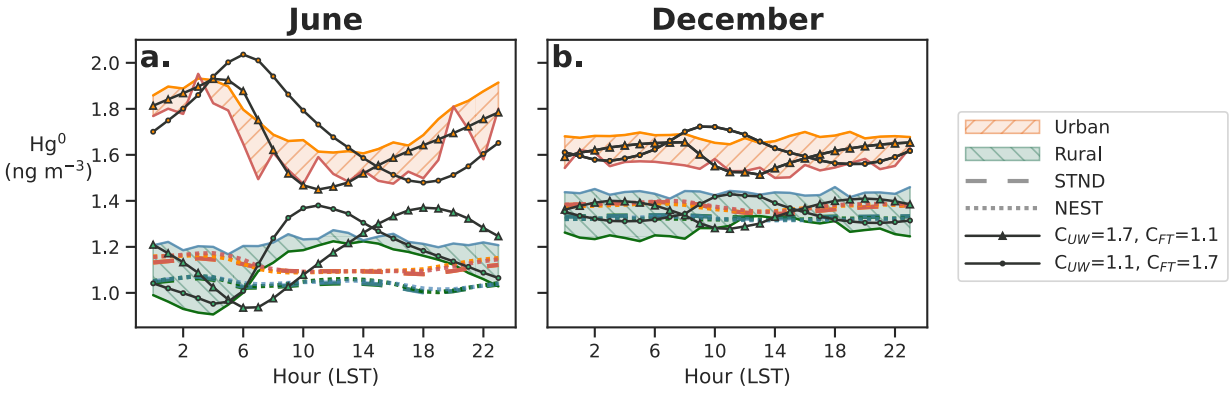

Figure 3. Comparison of the average diel variations of Hg^0 in measurements and models in June (a) and December (b). Solid colored lines represent the average diel variation at the four sites indicated in figure 2 for the respective month, and the area between these solid lines are shaded to represent the average range of concentrations in urban (orange shading) and rural (green shading)

regions. Diel variations simulated by the STND and NEST simulations for the grid boxes representing each of the four measurement sites are indicated by dashed and dotted lines, respectively. Diel variations obtained from our box model calibration approach are also overlayed for two illustrative combinations of C_{UW} and C_{FT}: C_{UW}=1.7 and C_{FT}=1.1 (triangle), and C_{UW}=1.1 and C_{FT}=1.7 (circle), where points are colored based on the region the model is calibrated to.

Diel variations of Hg^0 concentrations at sites within a given region and month are similar, but variations at rural and urban sites are out-of-phase (Figure 3). Concentrations at urban sites are highest at night and lowest at midday, while rural sites have the lowest concentrations before dawn and highest concentrations at midday. The consistency of concentration variations within regions provides confidence that these variations are regionally representative. A large concentration difference exists between urban and rural sites, with concentrations at rural sites 20-45% lower than the values measured at urban sites for respective hours. We find that the convergence of Hg^0 concentrations at urban and rural sites noted in Figure 2 consistently occurs at midday, particularly in June. Spatial gradients persist in December, with rural concentrations 12-18% lower than urban values and a negligible diel variation at all sites (Figure 3b). While concentrations at rural sites are between 10% (midday) and 21% (night) higher in December than in June, concentrations at the urban site are only 3% higher in December at midday and 20% lower on average during nocturnal hours. This seasonal difference largely reflects seasonal shifts in meteorological ventilation in the northeastern US, where stagnation and strong nocturnal inversions dominate during the summer and horizontal advection increases in the winter, thereby limiting the nocturnal buildup of concentrations (Figures S6-S8). These differences in seasonality are also consistent with previous findings that seasonal variability may reflect the influence of regional surface fluxes and meteorology[20].

293 Both STND and NEST simulations fail to capture the strong spatial and diel variability observed
294 at these four sites. In June, STND and NEST simulations underestimate observed concentrations
295 at all four sites during the day, and underestimate concentrations at urban sites at all hours,
296 exhibiting a negligible spatial gradient and minimal diel variation that is inconsistent with observed
297 patterns (Figure 3a). In December, STND and NEST simulations exhibit a muted diel variation
298 that is consistent with observations, however urban concentrations are underestimated at all hours
299 (Figure 3b). The STND and NEST simulations also predict a seasonal variation in concentration
300 magnitude that is generally consistent with average concentrations at rural sites. The nearly
301 identical performance of STND and NEST simulations indicates that biases are not driven by the
302 spatial smoothing induced by large grid cells.
303 We find that the contribution of chemical fluxes to diel variability in these regions is minor by
304 comparing simulated net and gross chemical fluxes within the PBL to net surface fluxes for the
305 NEST, ANT3, ANT7, and ANT10 simulations (Figure S24). These simulations estimate that net
306 chemical fluxes of Hg within the PBL in June are 36-875 times smaller than net surface fluxes
307 (normalized by average PBLH) at the rural sites and 21-30 times smaller at urban sites,
308 underscoring the secondary role of chemical fluxes on the short-term Hg^0 concentration variability
309 in this region. This is unsurprising given the long global lifetime Hg^0 against oxidation, which has
310 ranged between 2.3-4.5 months in recent versions of GEOS-Chem[6–8].
311 The secondary contribution of in-situ chemical processing to diel variability is further supported
312 by simulations of our boundary layer box model, which captures the qualitative characteristics of
313 diel variations in both urban and rural regions without considering fluxes from chemistry or short
314 term reservoirs (Figure 3). We demonstrate the result of our calibration technique by plotting the
315 resulting diel variations for the urban and rural cases assuming two illustrative combinations of

316 C_{UW} and C_{FT}. In June, we find that a constant surface flux of 12.6 ng m^{-2} hr^{-1} can best reproduce
317 the observed monthly average urban concentration given C_{UW}=1.7 ng m^{-3} and C_{FT}=1.1 ng m^{-3}, while
318 a constant flux of -26.9 ng m^{-2} hr^{-1} best reproduces the observed average rural concentration (Figure
319 3a). In December, we find that the box model bounded by the same values of C_{UW} and C_{FT} best
320 reproduces observed monthly average urban concentration with a constant flux of -1.8 ng m^{-2} hr^{-1},
321 while a flux of -30.5 ng m^{-2} hr^{-1} is required to reproduce the observed average rural concentration
322 (Figure 3b). Although surface fluxes are only optimized to reproduce the monthly average regional
323 concentration for the respective month, the boundary layer box model qualitatively reproduces
324 dominant characteristics of diel variability at both sites in both months, with previously noted out-
325 of-phase behavior in June and muted variations in December. For completeness, we also run the
326 box model while assuming that F_{Chem} is equivalent to the net chemical production of Hg^0 in the
327 GEOS-Chem model, finding that the net flux required to calibrate the box model was effectively
328 equivalent to the case when F_{Chem} was assumed to be zero (Figures S9-S10), which is consistent
329 with the minimal contribution of chemical fluxes shown in figure S24. We further underscore the
330 limited contribution of local redox chemistry to diel variability with an additional set of sensitivity
331 simulations where F_{Chem} is assumed to be equal to the net chemical loss of Hg according to the
332 GEOS-Chem model, which again does not notably impact the calibrated flux required to reproduce
333 observed loadings (Figure S11).

334 The diurnal convergence of Hg^0 concentrations across rural and urban regions in June highlights
335 the important influence of boundary layer entrainment on surface concentration variability. The
336 consistency of measurements within rural and urban regions provides confidence that the observed
337 diel variability is representative of the respective region rather than a measurement site artifact.
338 Figure 2 highlights that rural and urban sites consistently converge toward a common

concentration throughout the record, suggesting a mixing-driven control on concentrations. We find that Hg^0 concentrations consistently converge from dawn to midday and diverge later in the day, particularly in June. The timing of this convergence corresponds with the period of maximum ventilation (i.e., PBL growth and horizontal advection), while Hg^0 concentration divergence later in the day corresponds with PBL collapse and diminished advection (i.e., Figures S6-S8). Given the 400 km distance between sites, the communication of surface processes solely by horizontal advection is not possible, though we discuss this in more detail in section 3.3. This convergence suggests that spatial gradients of surface exchange and the communication of air within the PBL with background loadings in the free troposphere must drive observed diel variability. Given that net chemical fluxes in the rural and urban regions considered are 2-3 orders of magnitude smaller than net surface fluxes, we confirm the diminished role of in-situ chemical fluxes on diel Hg^0 variability suggested by other studies[17,27]. This is confirmed by our boundary layer box model, which qualitatively reproduces expected diel variations when forced by temporally invariant surface fluxes that are calibrated to reproduce monthly average concentrations.

3.2. Solution spaces of optimized fluxes in urban and rural regions

To account for the unknown magnitude of C_{FT} and C_{UW}, we repeat the box model optimization across a conservative range of C_{FT} and C_{UW} estimates (1-2 ng m^{-3}) for rural (Figure 4a) and urban (Figure 4b) regions. The shading in Figure 4 represents the constant surface flux that minimizes the residual of the model and the average monthly concentration in the respective region for a given combination of C_{FT} and C_{UW}, where blue colors indicate a negative (deposition) flux, and reds indicate a positive (emission) flux. The transition between positive and negative fluxes occurs at lower C_{FT} and C_{UW} for the rural case than the urban case, and in both cases follows a slope that suggests greater sensitivity to C_{UW} than C_{FT} at both sites. In both regions, larger emission fluxes

362 are required when boundary concentrations are low, while larger deposition fluxes are required
363 when boundary concentrations are high.

364 Observational constraints can be used to identify reasonable areas of the solution spaces. For
365 instance, if the midday convergence of Hg^0 concentrations in June is driven by the entrainment of
366 free tropospheric air during PBL growth, then the midday extrema in rural and urban sites should
367 approach the average regional value of C_{FT}. This allows us to ignore regions of the solution space
368 where C_{FT} is smaller than 1.25 ng m^{-3} or larger than 1.55 ng m^{-3} (Figure 4). We further constrain
369 the reasonable solution space by selecting areas where the diel concentration amplitude simulated
370 by the box model is within 50% of the average observed diel amplitude, which is indicated by the
371 dashed outlined regions (Figure 4). Finally, we restrict the observationally-constrained solution
372 space to negative values for the rural region and positive values for the urban region based on
373 source and sink behavior established by existing literature[22,30]. The final observationally-
374 constrained solution space for the rural region includes C_{UW} ranging from 1.0 to 1.5 ng m^{-3}, which
375 covers optimal fluxes between 0 – -15 ng m^{-2} hr^{-1}, while the urban case includes upwind
376 concentrations from 1.3-1.9 ng m^{-3} and average surface fluxes of 0-30 ng m^{-2} hr^{-1}.

377 The observationally constrained solution spaces described above indicate that NEST
378 underestimates transport fluxes in both rural and urban regions. We estimate C_{FT}, C_{UW}, and F for
379 the NEST simulation following the approach described in supplemental section S3.3 and plot the
380 location of this simulation within the solution space as the circular point in both panels of Figure
381 3. In the rural region, GEOS-Chem predicts a net average surface flux of -2.6 ng m^{-2} hr^{-1}, which is
382 consistent with the range of fluxes in the observationally constrained solution space. However,
383 NEST predicts C_{UW}=1.06 ng m^{-2} and C_{FT}=1.09 ng m^{-2}, which lie well outside of the observationally
384 constrained solution space. Similarly, the NEST simulation predicts an average surface flux of 1.4

ng m^{-2} hr^{-1} for the urban region that is consistent with fluxes in the constrained solution space but has boundary concentrations of C_{UW}=1.1 ng m^{-3} and C_{FT}=1.1 ng m^{-3}, again lying well outside of the observationally constrained solution space. We discuss sensitivity simulations that explore this solution space in section 3.3.

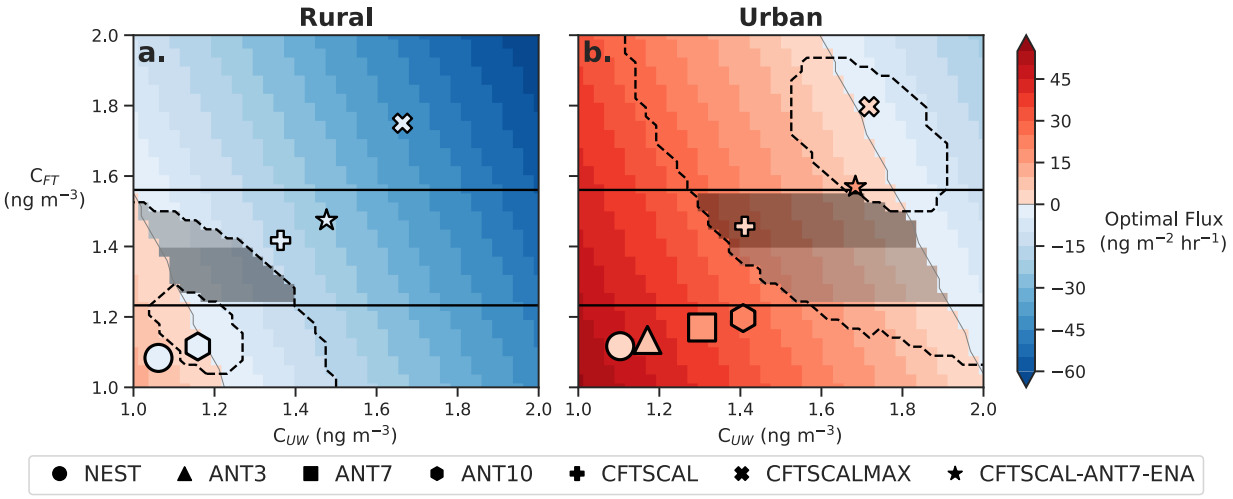

Figure 4. Solution space of the optimal flux for combinations of C_{UW} and C_{FT} from 1 ng m^{-3} to 2 ng m^{-3} in June for rural (a) and urban (b) regions. Horizontal solid lines refer to the likely bounds of C_{FT}, while dashed lines encompass the portion of the space where simulated diurnal amplitude is within 50% of the observed value. Gray shading outlines the observationally constrained solution space, with the heavy shading indicating the region with highest confidence. GEOS-Chem simulation results are overlaid based on estimated values C_{FT} and C_{UW} and F for the respective region.

We also use the box model to evaluate solution spaces for rural (Figure 5a) and urban (Figure 5b) sites in December. The threshold between positive and negative fluxes in the box model occurs at higher values of C_{UW} in the rural region and lower values of C_{UW} at the urban region. The flux threshold is also steeper than in June, suggesting a diminished influence of C_{FT} that is consistent with increased stability and stronger horizontal advection typical during midlatitude winter

(Figures S6-S8). The observationally constrained solution space is smaller than in June, which is driven by the limited diel variation of concentrations in December. Interestingly, average midday concentrations (i.e., our C_{FT} constraint) are notably higher in December at the rural sites but are only slightly higher at urban sites, suggesting that C_{FT} varies spatially. As in June, the average net flux within each region suggested by NEST is consistent with the observationally constrained solution space in both rural and urban regions, however C_{UW} and C_{FT} are notably lower than those in the constrained space.

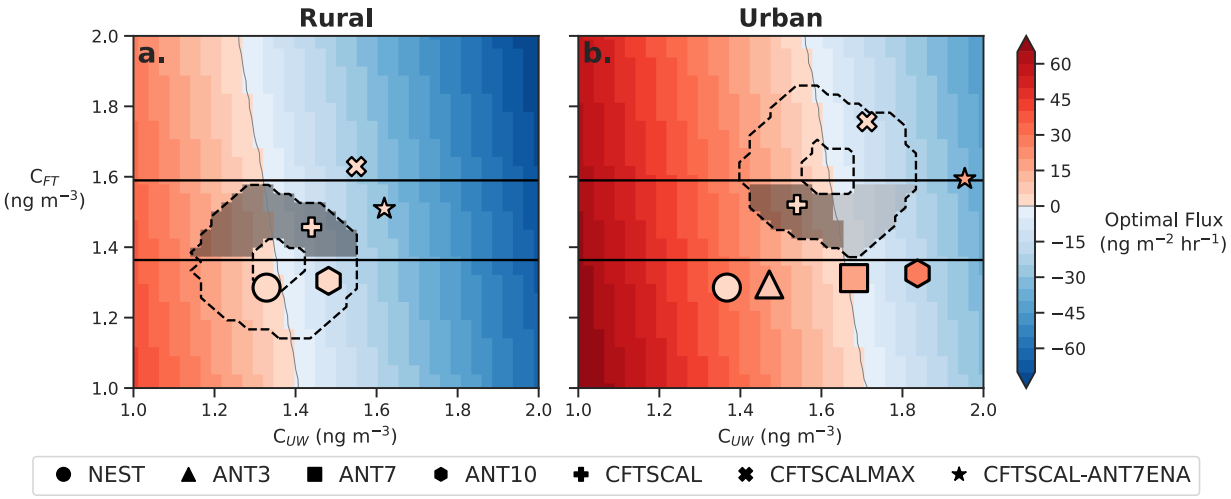

Figure 5. Solution space of the optimal flux for combinations of C_{UW} and C_{FT} from 1 ng m^{-3} to 2 ng m^{-3} in December for rural (a) and urban (b) regions. Horizontal solid lines refer to the likely bounds of C_{FT}, while dashed lines encompass the region of the space where simulated diurnal amplitude is within 50% of the observed value. Gray shading outlines the observationally constrained solution space, with the heavy shading indicating the region with highest confidence. GEOS-Chem simulation results are overlaid based on estimated values C_{FT} and C_{UW} and F for the respective region.

3.3. Impact of flux enhancement on diel variability

We evaluate a series of sensitivity simulations to determine whether enhancements to regional surface fluxes (i.e., F) or transport fluxes (driven by C_{FT} and C_{UW}) can allow GEOS-Chem to satisfy the observationally constrained solution space in June (Figure 4). We first evaluate the impact of regional surface flux enhancements using the ANT3, ANT7, and ANT10 simulations. These simulations scale anthropogenic emissions throughout the northeastern US (Figure 1, solid box), meaning that F, C_{UW}, and C_{FT} may be sensitive to changes (see supplemental section S3.3). As mentioned in section 2.2., we assume that these scaled emission scenarios represent the net impact of both primary anthropogenic emissions and the reemission of historical pollution, which will scale with population density. We find that scaling anthropogenic emissions by a factor of ten has little effect on the net regional flux in the rural region since there are limited anthropogenic emissions in this area (Figure 1) and surface fluxes are dominated by vegetative uptake. However, we find that this emission enhancement does lead to a 9% and 3% increase in the rural C_{UW} and C_{FT}, respectively. The same factor of ten anthropogenic emission enhancement has a larger effect on the net regional flux (encompassing all emission and deposition processes) in the urban region, increasing the net flux by a factor of 17 (23.9 ng m^{-2} hr^{-1}) and C_{UW} and C_{FT} by 27% and 7%, respectively. However, the C_{UW} and C_{FT} increases caused by this regional emission enhancement are insufficient to satisfy the observationally constrained solution space.

We also evaluate the impact of enhancements to regional C_{FT} in June using the CFTSCAL and CFTSCALMAX simulations in this region (Figure 4). C_{UW} is remarkably sensitive to C_{FT} in both urban and rural regions, and net surface fluxes are not notably impacted in either simulation. Our C_{FT} enhancements overshoot the constrained solution space for the rural region, however the strong linear response of the two simulations suggest that a value of C_{FT} that is higher than NEST but

lower than CFTSCAL in this region would move GEOS-Chem into the observationally constrained solution space. We observe a similar linear response to C_{FT} enhancements in the urban region and find that the CFTSCAL simulation moves GEOS-Chem into the optimally constrained solution space, albeit with a regional surface flux that is inconsistent with the underlying solution space. The strong linearity of the CFTSCAL and CFTSCALMAX simulations illustrates the important interaction of C_{UW} and C_{FT}, indicating that the reasonable range of possible combinations likely falls closer to the 1:1 line where $C_{UW} \approx C_{FT}$. Additionally, we find that the simultaneous enhancement of free tropospheric loadings and regional emissions in the CFTSCAL-ANT7-ENA simulation shifts the GEOS-Chem model into the observationally-constrained solution space in the urban region, but moves the model farther from the observationally-constrained space in the rural region due primarily to the overestimated values of C_{UW} and C_{FT}.

Regional emission enhancements are also insufficient for GEOS-Chem to satisfy the observationally constrained solution space in December. We find that C_{FT} has lower sensitivity to regional emission enhancements in December than in June, which is consistent with increased atmospheric stability in winter. As in June, C_{FT} enhancements also influence C_{UW}, with CFTSCAL shifting GEOS-Chem to the constrained solution space in rural and urban areas. However, net GEOS-Chem fluxes do not correspond with the underlying solution space, having the opposite sign in the rural case (Figure 5a) and being too weak in the urban case (Figure 5b). Similar to the rural region in June, we find that the CFTSCAL-ANT7-ENA simulation moves the GEOS-Chem model away from the constrained solution space in both rural and urban regions in December.

We evaluate the impact of enhancements to regional emissions or C_{FT} at urban and rural sites on diel variability in both June and December and find that neither alone are sufficient to reproduce observed patterns (Figures 6, S33). For instance, the regional emission enhancement explored in

the ANT7 simulation increased F, C_{UW}, and C_{FT} in the urban region (Figure 4), which we find results in a stronger diel variation with amplitude that is comparable to observations in June (Figure 6a), though this same simulation overestimates diel amplitude in December (Figure 6b). Meanwhile, the CFTSCAL simulation increases transport fluxes without affecting regional surface fluxes, which results in a uniform enhancement to concentrations in both June and December (Figures 6a and 6b, respectively, Figures S27, S30). This adjustment does not notably affect the concentration difference between rural and urban concentrations but has a strong impact on overall average concentrations. This highlights that neither regional emission enhancements nor C_{FT} enhancements alone can allow GEOS-Chem to reproduce observed spatial and diel variability. Instead, our modeling results demonstrate the complementary effects of these key fluxes, with surface fluxes primarily responsible for setting the amplitude of diel variations and C_{FT} primarily responsible for setting the daytime concentration extreme. This is further confirmed by the CFTSCAL-ANT7-ENA simulation, where regional emissions and C_{FT} are simultaneously adjusted to reproduce the diel variation of Hg^0 at the urban region in June. However, the failure of this sensitivity simulation to reproduce diel variability across all sites indicates that spatial variation in net surface fluxes and transport fluxes exist that are not adequately represented by this simple sensitivity simulation.

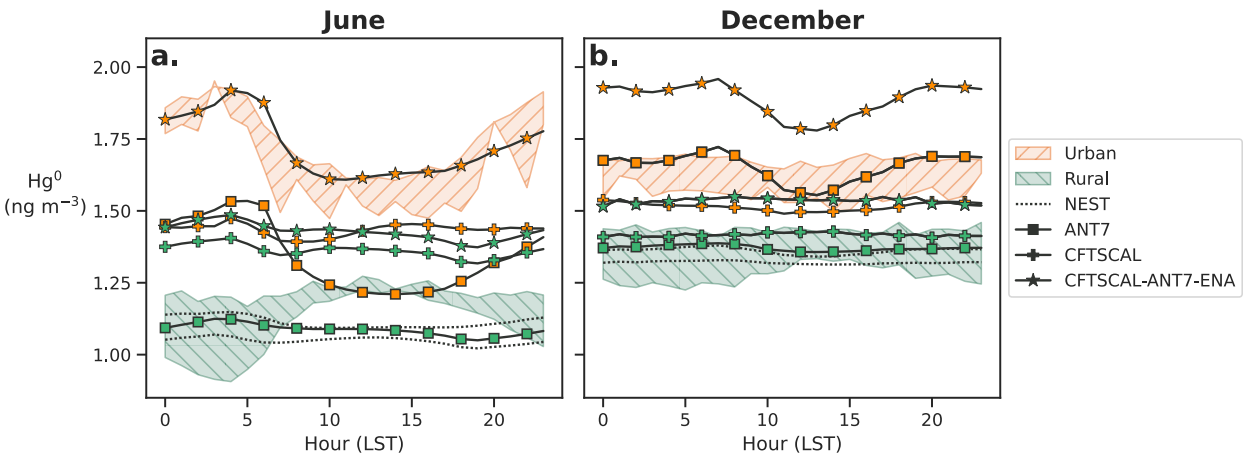

Figure 6. Comparison of diel variation of average regional observations in June (a) and December (b) with respective predictions from NEST, ANT7, CFTSCAL, and CFTSCAL-ANT7-ENA sensitivity simulations. Green and orange shaded regions corresponds with the average range of measured rural and urban concentrations (see figure 3). Similarly, diel variations from sensitivity simulations are colored to represent rural and urban regions, respectively.

It is worth noting that each GEOS-Chem simulation fails to reproduce the nocturnal concentration minimum observed at rural sites. This is likely caused by the existing parameterization of Hg^0 uptake in GEOS-Chem which is largely driven by incoming solar radiation[6], preventing the simulation of net nocturnal uptake suggested by recent observations[22,25,26,38]. As a result, modeled concentrations remain constant or increase slightly overnight, unlike declines implied by observations.

3.4. Implications for atmospheric modeling and monitoring

Our analysis shows that diel variations of Hg^0 concentrations can serve as a useful constraint on magnitude and temporal variation of regional free tropospheric concentrations, for which there are limited observations. The ranges of C_{FT} suggested by midday concentrations at urban and rural sites in June and December (1.25-1.55 ng m^{-3} and 1.35-1.60 ng m^{-3}, respectively) are consistent

500 with vertical profiles taken during an aircraft campaign in Tennessee in 2012 and 2013[39], where
501 summertime concentrations in the lower 5 km of the atmosphere ranged between 1.0-1.4 ng m^{-3} in
502 June and 1.25-1.6 ng m^{-3} in November and January. Given the expense of aircraft-based
503 measurements, we argue that existing ground-based measurements can be used to identify a useful
504 estimate of this concentration, which we show is critical for accurate representation of spatial and
505 temporal variability in CTMs. We expect this mechanism to hold in regions where surface fluxes
506 exert the dominant influence on Hg concentrations in the lower atmosphere, and where boundary
507 layer dynamics are primarily controlled by the diurnality of solar activity. As a result, we do not
508 expect this framework to be representative of atmospheric Hg dynamics in the Arctic, where rapid
509 chemical cycling drives atmospheric mercury depletion events. We also do not expect this
510 framework to be representative of marine environments, where diel PBLH variations are smaller
511 due to the reduced variation of sea surface temperatures when compared to land surfaces.
512 The spatial and temporal variability of surface Hg^0 concentrations at regional scales can be
513 largely explained by processes that should be able to be captured by global CTMs. Our simple
514 modeling exercise demonstrates that the daily variation of concentrations can be explained by the
515 interaction of regional surface fluxes and transport fluxes, rather than previously hypothesized
516 short-term reservoirs or local redox chemistry, which we would not expect to capture with
517 currently available CTMs. Therefore, we suggest that diel variability can serve as an additional
518 constraint to evaluate the mechanistic performance of CTMs.
519 The biases that we observe in urban and rural regions in our GEOS-Chem simulations imply that
520 the free tropospheric burden of Hg^0 in GEOS-Chem is underestimated, which may be addressed
521 by enhancing key global sources (emissions, reduction of Hg^{II}) or reducing key global sinks
522 (deposition, oxidation of Hg^0). While enhancing Hg^{II} reduction or reducing Hg^0 oxidation could

increase free tropospheric burdens of Hg^0, Shah et al.[8] found that the chemical mechanism currently used in GEOS-Chem also underestimates Hg^{II} loadings in the free troposphere, leading to underestimates of wet deposition. Hg^0 underestimates are also unlikely to be driven by excessive Hg^0 vegetative uptake, as a subsequent update to the GEOS-Chem model using direct observational constraints on this flux increased simulated annual Hg^0 deposition by 84%[6] when compared to the Shah et al. model.

Given these constraints, broadly distributed emission enhancements are the most likely explanation for the underestimate of the free tropospheric burden. We evaluate the impact of emission enhancements across broader spatial scales using the ANT3-ENA, ANT7-ENA, and ANT10-ENA sensitivity simulations, where emissions are scaled across eastern North America (Figure 1, Figures S31-S32). Using the strong linear response of C_{FT} to regional emission enhancements, we calculate the net regional flux required to reproduce the lower bound and central estimate of C_{FT} in June (1.25 and 1.45 ng m^{-3}, respectively). For sensitivity simulations where emission enhancements are only applied to the northeast US, emissions would need to be enhanced by a factor of 16 and 32 to reach these C_{FT} values, while emissions would need to be enhanced by a factor of 8 and 16 if enhancements are applied across eastern North America. Given the unlikely emission enhancements required over the northeastern US or eastern North America to satisfy observational constraints on C_{FT}, along with the associated unlikely enhancements to C_{UW}, smaller emission enhancements across continental or hemispheric scales are likely required.

Our findings demonstrate that diel variability can serve as a critical constraint on tropospheric Hg loadings in global CTMs that are used to evaluate environmental policy effectiveness, motivating continued support of temporally resolved Hg monitoring networks. This additional diagnostic tool could prove especially useful for evaluating model behavior and consistency in

546 ongoing intercomparison projects[40] that seek to reconcile observed atmospheric trends with current
547 estimates of anthropogenic emissions in support of international Hg policy.
548
549 CODE AND DATA AVAILABILITY
550 All code and model data required to reproduce the results presented in this study are published on
551 Zenodo (10.5281/zenodo.20432685)[41]. A preprint of this manuscript is posted on EarthArXiv
552 (10.31223/X52Z0P)[42].
553
554 ASSOCIATED CONTENT
555 *Supporting information*. Further supporting information can be found in the attached pdf.
556 AUTHOR INFORMATION
557 **Corresponding Author**
558 * Eric Roy – Department of Earth, Atmospheric, and Planetary Sciences, Massachusetts Institute
559 of Technology, Cambridge, MA, 02139, USA; https://orcid.org/0000-0002-3077-8011; Email:
560 emroy@mit.edu
561 ACKNOWLEDGMENT
562 We would like to acknowledge helpful conversations with Yuying Cui, Lexia Cicone, and Connor
563 Olsen. This research was made possible by United States National Science Foundation grant
564 #1924148, the MIT Department of Earth, Atmospheric, and Planetary Sciences Charney
565 Fellowship. This publication was made possible by the generous support of the Government of
566 Portugal through the Portuguese Foundation for International Cooperation in Science, Technology
567 and Higher Education and was undertaken in MIT Portugal Program.
568
569
570

GRAPHICAL ABSTRACT

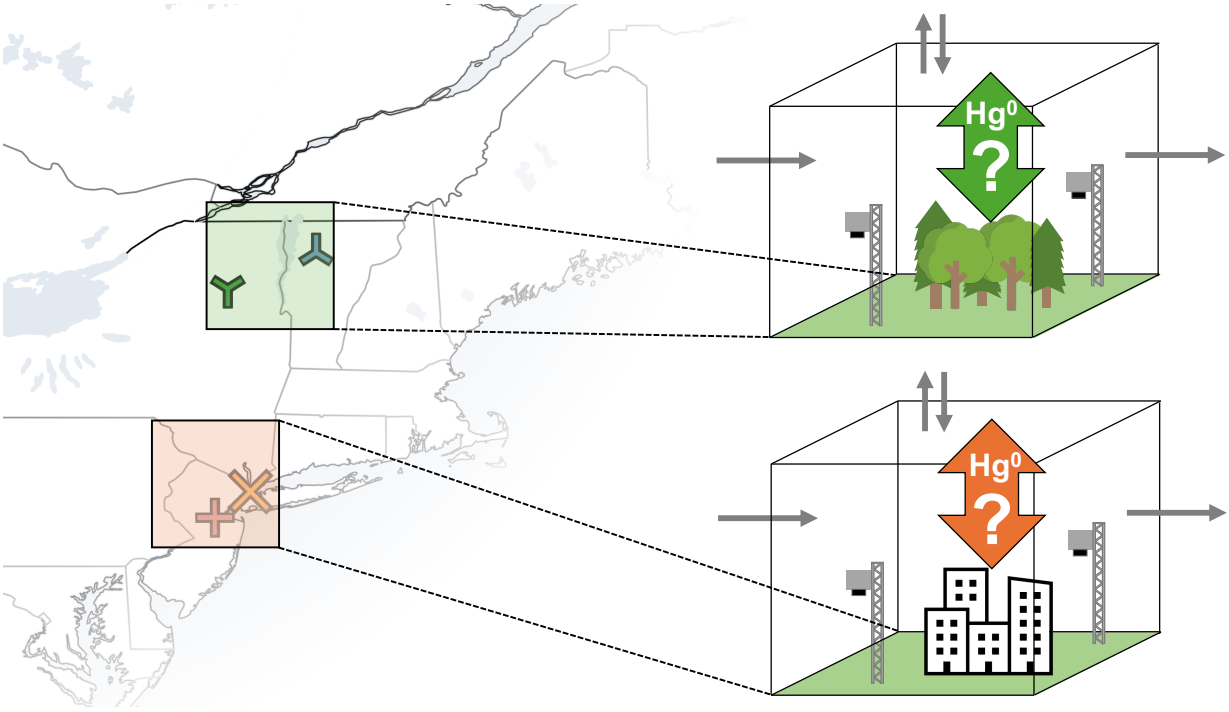

REFERENCES

(1) Basu, N.; Bastiansz, A.; Dórea, J. G.; Fujimura, M.; Horvat, M.; Shroff, E.; Weihe, P.; Zastenskaya, I. Our Evolved Understanding of the Human Health Risks of Mercury. *Ambio* **2023**, *52* (5), 877–896. https://doi.org/10.1007/s13280-023-01831-6.

(2) Hsu-Kim, H.; Eckley, C. S.; Achá, D.; Feng, X.; Gilmour, C. C.; Jonsson, S.; Mitchell, C. P. J. Challenges and Opportunities for Managing Aquatic Mercury Pollution in Altered Landscapes. *Ambio* **2018**, *47* (2), 141–169. https://doi.org/10.1007/s13280-017-1006-7.

(3) Driscoll, C. T.; Mason, R. P.; Chan, H. M.; Jacob, D. J.; Pirrone, N. Mercury as a Global Pollutant: Sources, Pathways, and Effects. *Environ. Sci. Technol.* **2013**, *47* (10), 4967–4983. https://doi.org/10.1021/es305071v.

(4) Amos, H. M.; Jacob, D. J.; Streets, D. G.; Sunderland, E. M. Legacy Impacts of All-Time Anthropogenic Emissions on the Global Mercury Cycle. *Glob. Biogeochem. Cycles* **2013**, *27* (2), 410–421. https://doi.org/10.1002/gbc.20040.

(5) Geyman, B. M.; Streets, D. G.; Olson, C. I.; Thackray, C. P.; Olson, C. L.; Schaefer, K.; Krabbenhoft, D. P.; Sunderland, E. M. Cumulative Anthropogenic Impacts of Past and Future Emissions and Releases on the Global Mercury Cycle. *Environ. Sci. Technol.* **2025**, *59* (17), 8578–8590. https://doi.org/10.1021/acs.est.4c13434.

(6) Feinberg, A.; Dlamini, T.; Jiskra, M.; Shah, V.; Selin, N. E. Evaluating Atmospheric Mercury (Hg) Uptake by Vegetation in a Chemistry-Transport Model. *Environ. Sci. Process. Impacts* **2022**, *24* (9), 1303–1318. https://doi.org/10.1039/D2EM00032F.

(7) Horowitz, H. M.; Jacob, D. J.; Zhang, Y.; Dibble, T. S.; Slemr, F.; Amos, H. M.; Schmidt, J. A.; Corbitt, E. S.; Marais, E. A.; Sunderland, E. M. A New Mechanism for Atmospheric Mercury Redox Chemistry: Implications for the Global Mercury Budget. *Atmos. Chem. Phys.* **2017**, *17* (10), 6353–6371. https://doi.org/10.5194/acp-17-6353-2017.

(8) Shah, V.; Jacob, D. J.; Thackray, C. P.; Wang, X.; Sunderland, E. M.; Dibble, T. S.; Saiz-Lopez, A.; Černušák, I.; Kellö, V.; Castro, P. J.; Wu, R.; Wang, C. Improved Mechanistic Model of the Atmospheric Redox Chemistry of Mercury. *Environ. Sci. Technol.* **2021**, *55* (21), 14445–14456. https://doi.org/10.1021/acs.est.1c03160.
(9) Zhou, J.; Obrist, D.; Dastoor, A.; Jiskra, M.; Ryjkov, A. Vegetation Uptake of Mercury and Impacts on Global Cycling. *Nat. Rev. Earth Environ.* **2021**, *2* (4), 269–284. https://doi.org/10.1038/s43017-021-00146-y.
(10) Gustin, M. S.; Dunham-Cheatham, S. M.; Osterwalder, S.; Magand, O.; Dommergue, A. What Is the Utility of Measuring Gaseous HgII Dry Deposition Using Aerohead Samplers?: A Review. *Sci. Total Environ.* **2024**, *907*, 167895. https://doi.org/10.1016/j.scitotenv.2023.167895.
(11) Prestbo, E. M.; Gay, D. A. Wet Deposition of Mercury in the U.S. and Canada, 1996–2005: Results and Analysis of the NADP Mercury Deposition Network (MDN). *Atmos. Environ.* **2009**, *43* (27), 4223–4233. https://doi.org/10.1016/j.atmosenv.2009.05.028.
(12) Saiz-Lopez, A.; Sitkiewicz, S. P.; Roca-Sanjuán, D.; Oliva-Enrich, J. M.; Dávalos, J. Z.; Notario, R.; Jiskra, M.; Xu, Y.; Wang, F.; Thackray, C. P.; Sunderland, E. M.; Jacob, D. J.; Travnikov, O.; Cuevas, C. A.; Acuña, A. U.; Rivero, D.; Plane, J. M. C.; Kinnison, D. E.; Sonke, J. E. Photoreduction of Gaseous Oxidized Mercury Changes Global Atmospheric Mercury Speciation, Transport and Deposition. *Nat. Commun.* **2018**, *9* (1), 4796. https://doi.org/10.1038/s41467-018-07075-3.
(13) Gay, D. A.; Schmeltz, D.; Prestbo, E.; Olson, M.; Sharac, T.; Tordon, R. The Atmospheric Mercury Network: Measurement and Initial Examination of an Ongoing Atmospheric Mercury Record across North America. *Atmos. Chem. Phys.* **2013**, *13* (22), 11339–11349. https://doi.org/10.5194/acp-13-11339-2013.
(14) Sprovieri, F.; Pirrone, N.; Bencardino, M.; D'Amore, F.; Carbone, F.; Cinnirella, S.; Mannarino, V.; Landis, M.; Ebinghaus, R.; Weigelt, A.; Brunke, E.-G.; Labuschagne, C.; Martin, L.; Munthe, J.; Wängberg, I.; Artaxo, P.; Morais, F.; Barbosa, H. D. M. J.; Brito, J.; Cairns, W.; Barbante, C.; Diéguez, M. D. C.; Garcia, P. E.; Dommergue, A.; Angot, H.; Magand, O.; Skov, H.; Horvat, M.; Kotnik, J.; Read, K. A.; Neves, L. M.; Gawlik, B. M.; Sena, F.; Mashyanov, N.; Obolkin, V.; Wip, D.; Feng, X. B.; Zhang, H.; Fu, X.; Ramachandran, R.; Cossa, D.; Knoery, J.; Marusczak, N.; Nerentorp, M.; Norstrom, C. Atmospheric Mercury Concentrations Observed at Ground-Based Monitoring Sites Globally Distributed in the Framework of the GMOS Network. *Atmos. Chem. Phys.* **2016**, *16* (18), 11915–11935. https://doi.org/10.5194/acp-16-11915-2016.
(15) Stamenkovic, J.; Lyman, S.; Gustin, M. S. Seasonal and Diel Variation of Atmospheric Mercury Concentrations in the Reno (Nevada, USA) Airshed. *Atmos. Environ.* **2007**, *41* (31), 6662–6672. https://doi.org/10.1016/j.atmosenv.2007.04.015.
(16) Mao, H.; Cheng, I.; Zhang, L. Current Understanding of the Driving Mechanisms for Spatiotemporalvariations of Atmospheric Speciated Mercury: A Review. *Atmos. Chem. Phys.* **2016**, *16* (20), 12897–12924. https://doi.org/10.5194/acp-16-12897-2016.
(17) Lyman, S. N.; Elgiar, T.; Gustin, M. S.; Dunham-Cheatham, S. M.; David, L. M.; Zhang, L. Evidence against Rapid Mercury Oxidation in Photochemical Smog. *Environ. Sci. Technol.* **2022**, *56* (16), 11225–11235. https://doi.org/10.1021/acs.est.2c02224.
(18) Lan, X.; Talbot, R.; Castro, M.; Perry, K.; Luke, W. Seasonal and Diurnal Variations of Atmospheric Mercury across the US Determined from AMNet Monitoring Data. *Atmos. Chem. Phys.* **2012**, *12* (21), 10569–10582. https://doi.org/10.5194/acp-12-10569-2012.

(19) Nair, U. S.; Wu, Y.; Walters, J.; Jansen, J.; Edgerton, E. S. Diurnal and Seasonal Variation of Mercury Species at Coastal-Suburban, Urban, and Rural Sites in the Southeastern United States. *Atmos. Environ.* **2012**, *47*, 499–508. https://doi.org/10.1016/j.atmosenv.2011.09.056.
(20) Roy, E. M.; Zhou, J.; Wania, F.; Obrist, D. Use of Atmospheric Concentrations and Passive Samplers to Assess Surface-Atmosphere Exchange of Gaseous Mercury in Forests. *Chemosphere* **2023**, *341*, 140113. https://doi.org/10.1016/j.chemosphere.2023.140113.
(21) Jiskra, M.; Sonke, J. E.; Obrist, D.; Bieser, J.; Ebinghaus, R.; Myhre, C. L.; Pfaffhuber, K. A.; Wängberg, I.; Kyllönen, K.; Worthy, D.; Martin, L. G.; Labuschagne, C.; Mkololo, T.; Ramonet, M.; Magand, O.; Dommergue, A. A Vegetation Control on Seasonal Variations in Global Atmospheric Mercury Concentrations. *Nat. Geosci.* **2018**, *11* (4), 244–250. https://doi.org/10.1038/s41561-018-0078-8.
(22) Obrist, D.; Roy, E. M.; Harrison, J. L.; Kwong, C. F.; Munger, J. W.; Moosmüller, H.; Romero, C. D.; Sun, S.; Zhou, J.; Commane, R. Previously Unaccounted Atmospheric Mercury Deposition in a Midlatitude Deciduous Forest. *Proc. Natl. Acad. Sci.* **2021**, *118* (29), e2105477118. https://doi.org/10.1073/pnas.2105477118.
(23) St. Louis, V. L.; Graydon, J. A.; Lehnherr, I.; Amos, H. M.; Sunderland, E. M.; St. Pierre, K. A.; Emmerton, C. A.; Sandilands, K.; Tate, M.; Steffen, A.; Humphreys, E. R. Atmospheric Concentrations and Wet/Dry Loadings of Mercury at the Remote Experimental Lakes Area, Northwestern Ontario, Canada. *Environ. Sci. Technol.* **2019**, *53* (14), 8017–8026. https://doi.org/10.1021/acs.est.9b01338.
(24) Howard, D.; Edwards, G. C. Mercury Fluxes over an Australian Alpine Grassland and Observation of Nocturnal Atmospheric Mercury Depletion Events. *Atmos. Chem. Phys.* **2018**, *18* (1), 129–142. https://doi.org/10.5194/acp-18-129-2018.
(25) Zhou, J.; Bollen, S. W.; Roy, E. M.; Hollinger, D. Y.; Wang, T.; Lee, J. T.; Obrist, D. Comparing Ecosystem Gaseous Elemental Mercury Fluxes over a Deciduous and Coniferous Forest. *Nat. Commun.* **2023**, *14* (1), 2722. https://doi.org/10.1038/s41467-023-38225-x.
(26) Denzler, B.; Eugster, W.; Bogdal, C.; Bishop, K.; Buchmann, N.; Hungerbühler, K.; Osterwalder, S. Uptake of Gaseous Elemental Mercury by a Rainforest: Insights from a Tropical Glasshouse Used as a Dynamic Flux Chamber. *Environ. Sci. Technol.* **2025**, *59* (35), 18675–18686. https://doi.org/10.1021/acs.est.5c05823.
(27) Denzler, B.; Bogdal, C.; Kern, C.; Tobler, A.; Huo, J.; Hungerbühler, K. Urban Source Term Estimation for Mercury Using a Boundary-Layer Budget Method. *Atmos Chem Phys* **2019**.
(28) Gustin, M. S.; Dunham-Cheatham, S. M.; Lyman, S.; Horvat, M.; Gay, D. A.; Gačnik, J.; Gratz, L.; Kempkes, G.; Khalizov, A.; Lin, C.-J.; Lindberg, S. E.; Lown, L.; Martin, L.; Mason, R. P.; MacSween, K.; Vijayakumaran Nair, S.; Nguyen, L. S. P.; O'Neil, T.; Sommar, J.; Weiss-Penzias, P.; Zhang, L.; Živković, I. Measurement of Atmospheric Mercury: Current Limitations and Suggestions for Paths Forward. *Environ. Sci. Technol.* **2024**, *58* (29), 12853–12864. https://doi.org/10.1021/acs.est.4c06011.
(29) US Environmental Protection Agency. USEPA 2020 National Emissions Inventory, 2023.
(30) Aucott, M. L.; Caldarelli, A. D.; Zsolway, R. R.; Pietarinen, C. B.; England, R. Ambient Elemental, Reactive Gaseous, and Particle-Bound Mercury Concentrations in New Jersey, U.S.: Measurements and Associations with Wind Direction. *Environ. Monit. Assess.* **2009**, *158* (1–4), 295–306. https://doi.org/10.1007/s10661-008-0583-0.
(31) Steenhuisen, F.; Wilson, S. J. Development and Application of an Updated Geospatial Distribution Model for Gridding 2015 Global Mercury Emissions. *Atmos. Environ.* **2019**, *211*, 138–150. https://doi.org/10.1016/j.atmosenv.2019.05.003.

(32) Li, Y.; Martin, R. V.; Li, C.; Boys, B. L.; van Donkelaar, A.; Meng, J.; Pierce, J. R. Development and Evaluation of Processes Affecting Simulation of Diel Fine Particulate Matter Variation in the GEOS-Chem Model. *Atmos. Chem. Phys.* **2023**, *23* (19), 12525–12543. https://doi.org/10.5194/acp-23-12525-2023.
(33) Angot, H.; Rutkowski, E.; Sargent, M.; Wofsy, S. C.; Hutyra, L. R.; Howard, D.; Obrist, D.; Selin, N. E. Atmospheric Mercury Sources in a Coastal-Urban Environment: A Case Study in Boston, Massachusetts, USA. *Environ. Sci. Process. Impacts* **2021**, *23* (12), 1914–1929. https://doi.org/10.1039/D1EM00253H.
(34) Li, D. AMDAR_BL_PBLH_DATASET, 2020. https://doi.org/10.5281/ZENODO.3934377.
(35) Zhang, Y.; Sun, K.; Gao, Z.; Pan, Z.; Shook, M. A.; Li, D. Diurnal Climatology of Planetary Boundary Layer Height Over the Contiguous United States Derived From AMDAR and Reanalysis Data. *J. Geophys. Res. Atmos.* **2020**, *125* (20), e2020JD032803. https://doi.org/10.1029/2020JD032803.
(36) Seinfeld, J. H.; Pandis, S. N. *Atmospheric Chemistry and Physics: From Air Pollution to Climate Change*, Third edition.; John Wiley & Sons: Hoboken, New Jersey, 2016.
(37) Denning, A. S.; Takahashi, T.; Friedlingstein, P. Can a Strong Atmospheric CO_2 Rectifier Effect Be Reconciled with a “Reasonable” Carbon Budget? *Tellus B Chem. Phys. Meteorol.* **1999**, *51* (2), 249. https://doi.org/10.3402/tellusb.v51i2.16277.
(38) Khan, T. R.; Obrist, D.; Agnan, Y.; Selin, N. E.; Perlinger, J. A. Atmosphere-Terrestrial Exchange of Gaseous Elemental Mercury: Parameterization Improvement through Direct Comparison with Measured Ecosystem Fluxes. *Environ. Sci. Process. Impacts* **2019**, *21* (10), 1699–1712. https://doi.org/10.1039/C9EM00341J.
(39) Brooks, S.; Ren, X.; Cohen, M.; Luke, W.; Kelley, P.; Artz, R.; Hynes, A.; Landing, W.; Martos, B. Airborne Vertical Profiling of Mercury Speciation near Tullahoma, TN, USA. *Atmosphere* **2014**, *5* (3), 557–574. https://doi.org/10.3390/atmos5030557.
(40) Dastoor, A.; Angot, H.; Bieser, J.; Brocza, F.; Edwards, B.; Feinberg, A.; Feng, X.; Geyman, B.; Gournia, C.; He, Y.; Hedgecock, I. M.; Ilyin, I.; Kirk, J.; Lin, C.-J.; Lehnherr, I.; Mason, R.; McLagan, D.; Muntean, M.; Rafaj, P.; Roy, E. M.; Ryjkov, A.; Selin, N. E.; De Simone, F.; Soerensen, A. L.; Steenhuisen, F.; Travnikov, O.; Wang, S.; Wang, X.; Wilson, S.; Wu, R.; Wu, Q.; Zhang, Y.; Zhou, J.; Zhu, W.; Zolkos, S. The Multi-Compartment Hg Modeling and Analysis Project (MCHgMAP): Mercury Modeling to Support International Environmental Policy. *Geosci. Model Dev.* **2025**, *18* (9), 2747–2860. https://doi.org/10.5194/gmd-18-2747-2025.
(41) Roy, E.; Selin, N. Data and Code for Publication: "Spatially and Temporally Dense Measurements Reveal Meteorological Driver of Atmospheric Mercury Variability," 2026. https://doi.org/10.5281/ZENODO.20432685.
(42) Roy, E. M.; Gay, D. A.; Selin, N. E. Spatially and Temporally Dense Measurements Reveal Meteorological Driver of Atmospheric Mercury Variability. EarthArXiv June 2, 2026. https://doi.org/https://doi.org/10.31223/X52Z0P.

SUPPORTING INFORMATION

Regionally representative observations reveal coupled influence of meteorology and surface exchange on atmospheric mercury variability

Eric M. Roy[1,2]*, David A. Gay[3], Noelle E. Selin[1,2,4]

[1]Department of Earth, Atmospheric, and Planetary Sciences, Massachusetts Institute of Technology, Cambridge, MA 02139, USA

[2]Center for Sustainability Science and Strategy, Massachusetts Institute of Technology, Cambridge, MA 02139, USA

[3]National Atmospheric Deposition Program, Wisconsin State Laboratory of Hygiene, University of Wisconsin Madison, Madison, WI 53706, USA

[4]Institute for Data, Systems, and Society, Massachusetts Institute of Technology, Cambridge, MA 02139, USA

*Corresponding author: Eric M. Roy, Email: emroy@mit.edu

Number of pages: 27
Number of sections: 3
Number of tables: 4
Number of figures: 33

Table of Contents

S1. Observational Analysis

S1.1. NADP Observation Site characteristics and validation

Table S1. NADP Observational Site Characteristics*

Site name	Site code	Start date	End Date	NADP Site classification	Elevation (m)	Latitude (º)	Longitude (º)
Huntington Wildlife	NY20	Nov 2007	-	Isolated	500	43.97	-74.22
Underhill	VT99	Jan 2008	Jan 2016	Rural	399	44.53	-72.88
The Bronx	NY06	Jan 2016	Jun 2020	Urban	68	40.87	-73.88
New Brunswick	NJ30	Oct 2015	-	Urban	21	40.47	-74.42
Elizabeth Lab	NJ54	Oct 2015	-	Urban	11	40.64	-74.21

*Site characteristics accessed from https://nadp.slh.wisc.edu/amnet-site-list/ on August 18, 2026

S1.2. Hg^0 concentrations at Elizabeth, NJ (NJ54)

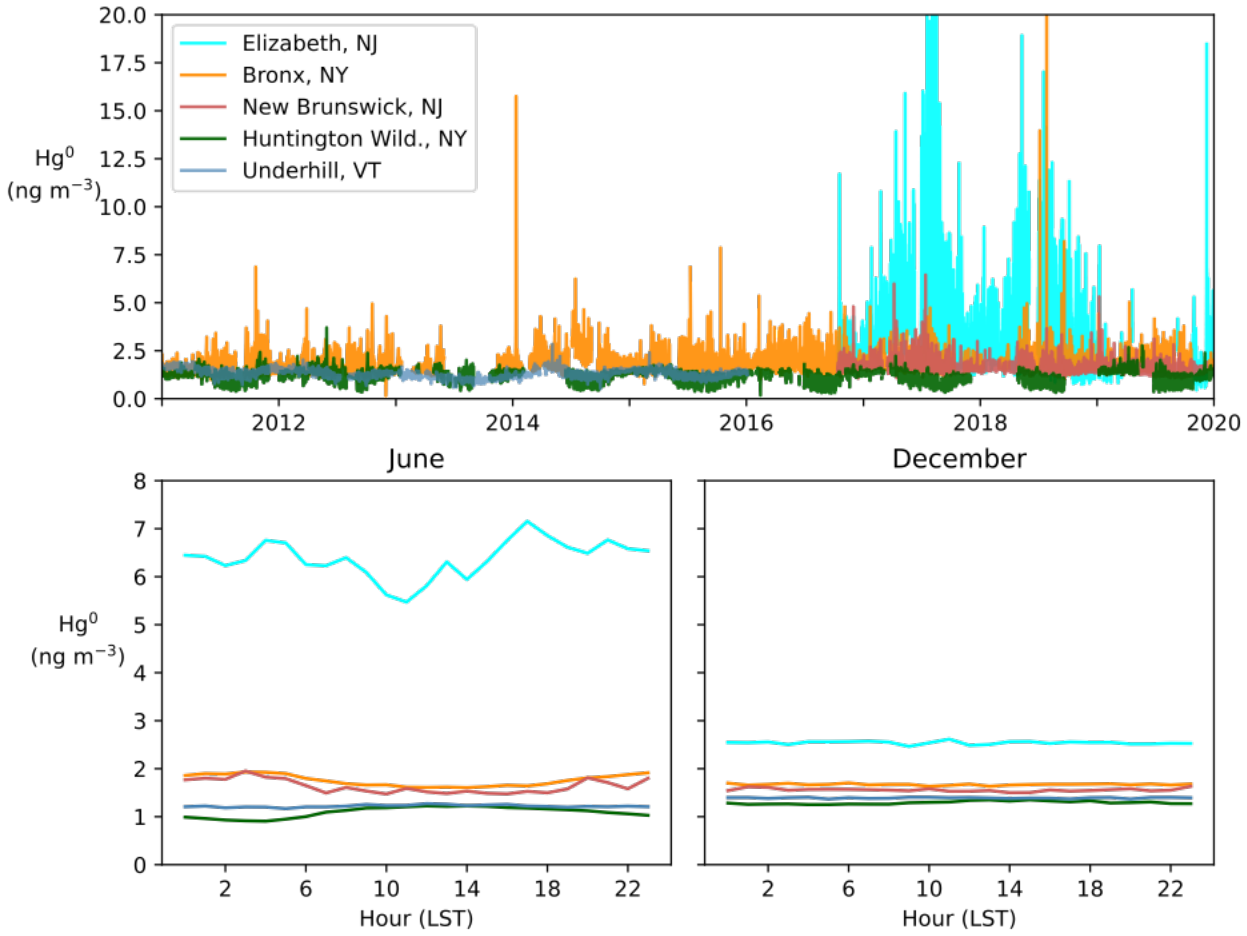

Figure S1. (top) Hourly concentrations at the four sites of interest, here including measurements at Elizabeth, NJ. Concentrations are notably higher at this site, even compared to The Bronx and New Brunswick. Average concentrations for each hour of the day during June (bottom left) are more than twice as high as other urban sites. Hourly average concentrations during December do not exhibit any notable diel cycle but remain notably higher than all other sites, further underscoring the likelihood that local sources exert a dominating influence on variability.

S1.3. Statistical comparison of observations

We formally establish the regional relationship of measurements by calculating the correlations between individual sites. We first evaluate the correlation of individual hourly measurements across sites where timeseries overlap in Figure S2. Notice that correlation coefficients are not evaluated between the New Brunswick, NJ sites and the Underhill, VT sites, as these two timeseries do not overlap. As expected, the strongest positive correlations in June are between rural sites (0.4) and urban sites (0.34), while correlations between sites in different region types are close to zero. Meanwhile, we find that correlations across nearly all sites are positive in December, with the strongest positive correlations between the two urban sites, and New Brunswick, NJ (0.27) and Huntington Wildlife, NY (0.34). This relationship is reasonable given increasing importance of synoptic scale transport in the midlatitudes in winter, along with the

generally muted variability at all four sites shown in Figure 3 of the main text. Despite exhibiting relatively weak correlation coefficients, the positive correlations of overlapping hourly concentrations of sites within a region, particularly in June, illustrates that the temporal variation of these sites is influenced by regional scale processes.

We also evaluate the correlation coefficients of our diurnally averaged profiles in Figure S3. We find strong positive correlation between sites within urban and rural regions in June, and strong negative correlations between sites in different regions. Correlations are near zero between most sites in December, except between the urban sites and Huntington Wildlife, NY, as that site continues to exhibit a midday peak in winter, albeit weaker than in summer. The increase in strength of these correlations between Figures S2 and S3 illustrates a key benefit of having spatially and temporally overlapping measurements for several years, as dominant modes of variability can be extracted from otherwise noisy measurement records.

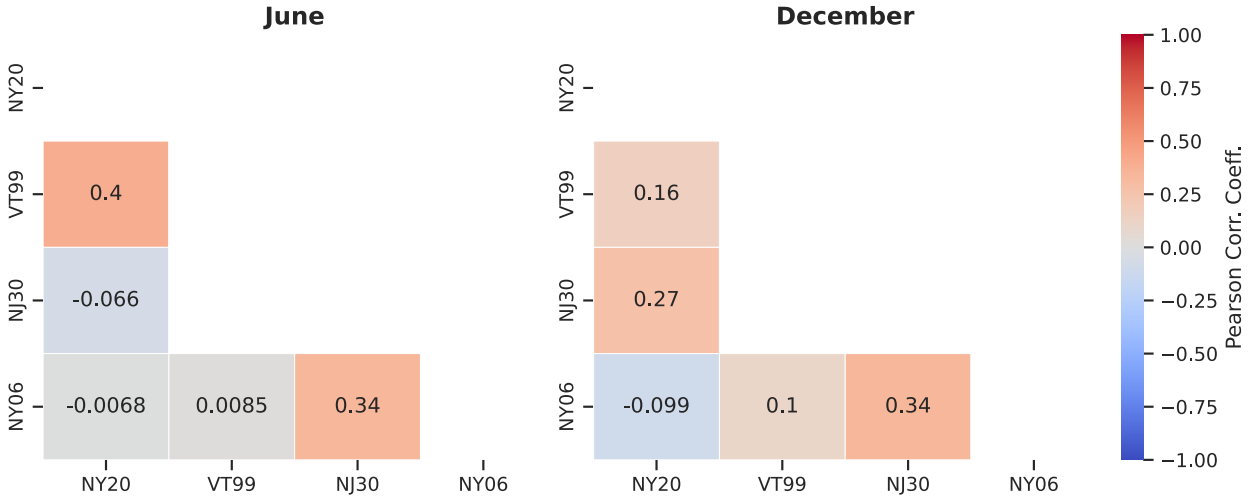

Figure S2. Cross correlations of hourly observations at the four measurement sites considered for June and December. Sites are referred to by their site codes; NY20: Huntington Wildlife, NY; VT99: Underhill, VT; NJ30: New Brunswick, NJ; and NY06: The Bronx, NY. Correlation between New Brunswick, NJ and Underhill, VT is not evaluated since records do not overlap.

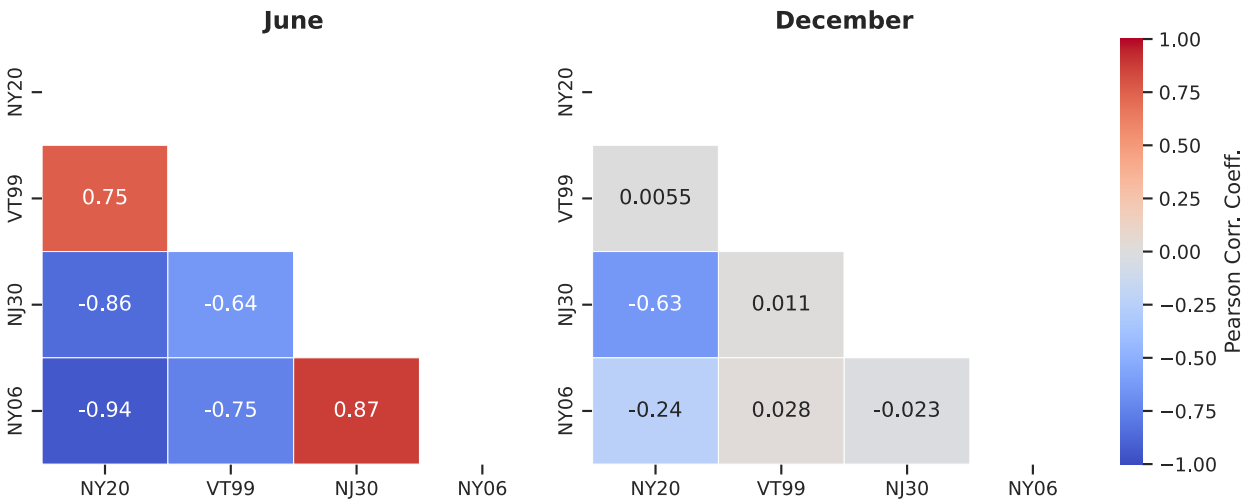

Figure S3. Cross correlations of average diel profile measurements at the four measurement sites considered for June and December. Sites are referred to by their site codes; NY20: Huntington Wildlife, NY; VT99: Underhill, VT; NJ30: New Brunswick, NJ; and NY06: The Bronx, NY.

S1.4. Interannual and seasonal validation of observations

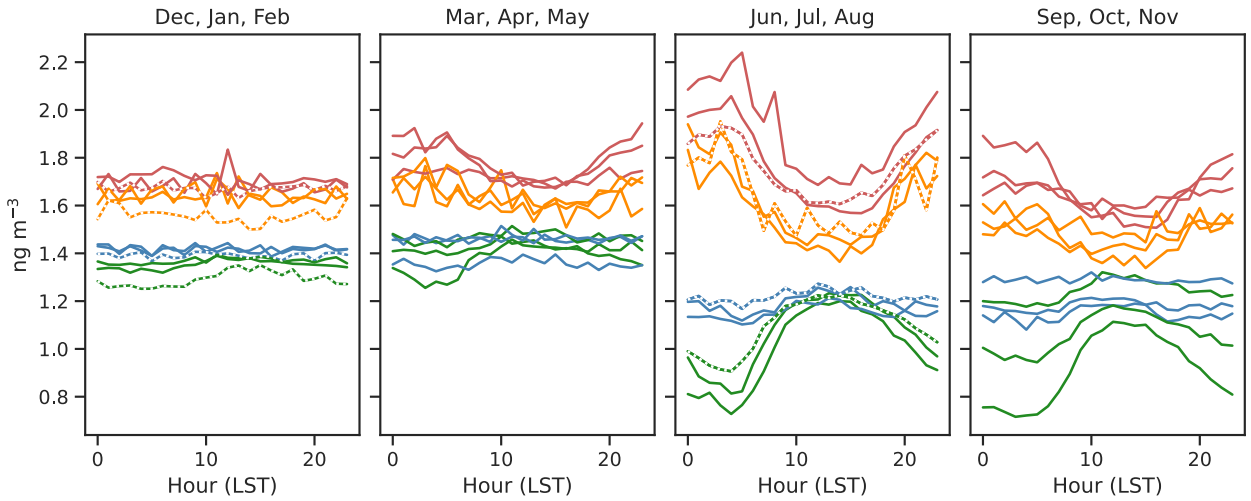

Figure S4. Average diel variation for each month and each site. Months investigated in the main text are overlayed with a dotted white line, with December included in the leftmost panel, and June included in the second panel from right.

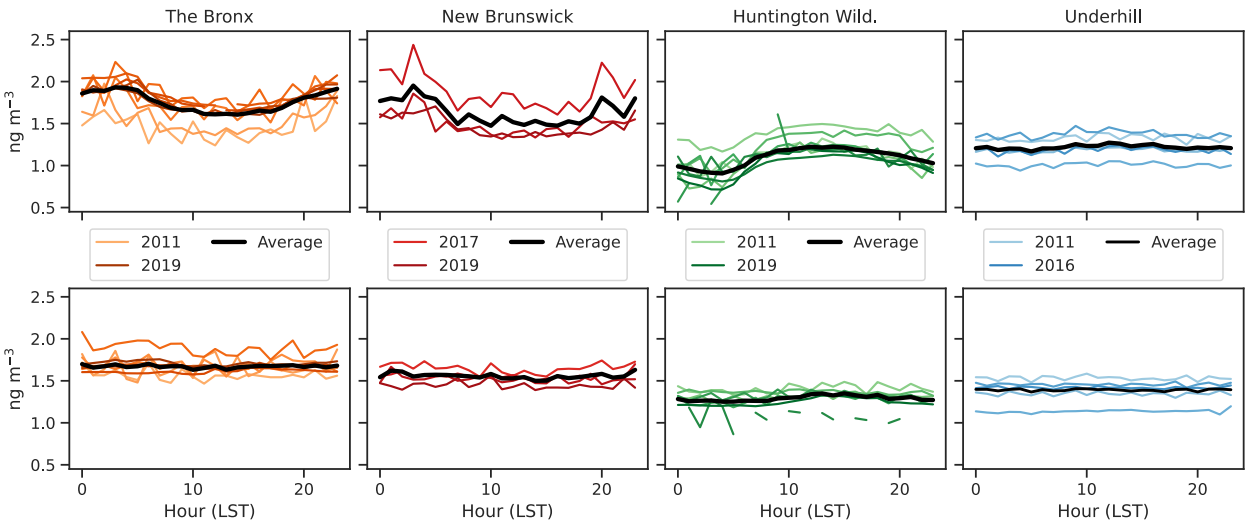

Figure S5. Diel variations in June (top row) and December (bottom row) for each year at all four sites. Shading corresponds with the respective year, with lighter colors corresponding with earlier years, while darker colors correspond with more recent years. The average diel variation at each site that is used throughout the main text is plotted in black. While interannual variations in concentrations across this time period exist, we do not observe a systematic year-over-year bias in the characteristics of diel variability.

S2. Box Model Analysis

Section S2.1. Evaluation of PBLH data used to drive boundary layer box model

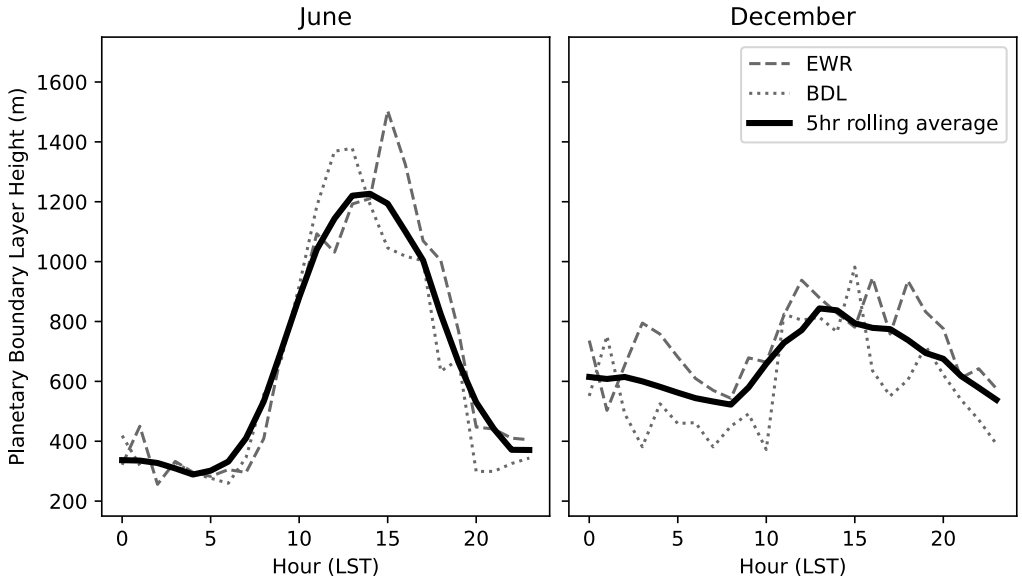

Figure S6. Comparison of PBLH from hourly data from Newark-Liberty International Airport (EWR) and Bradley International Airport (BDL) for June (left) and December (right) 2017. Average monthly PBLH is defined as the five-hour centered rolling average of these data, plotted as the solid black curve.

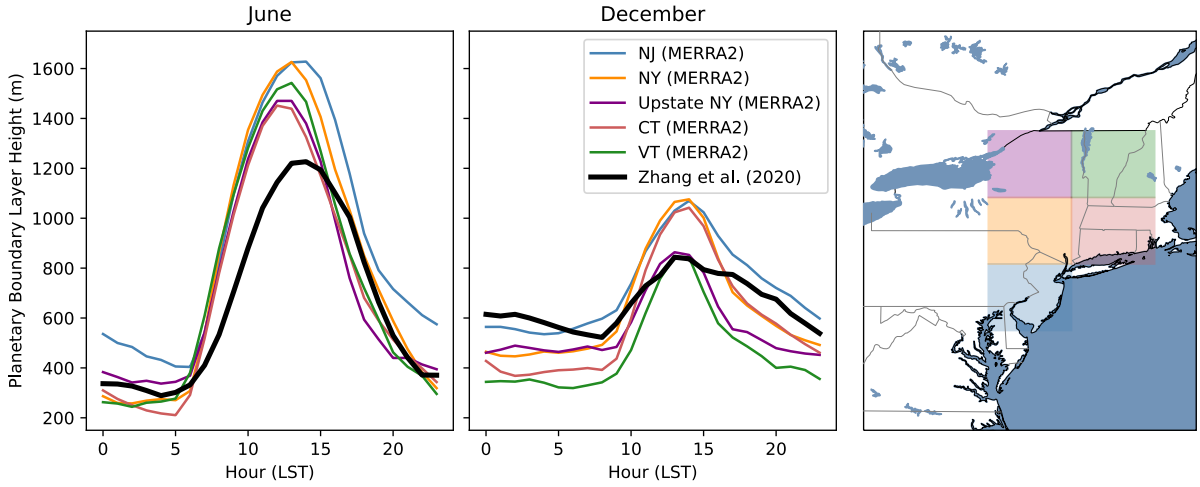

Figure S7. Average diurnal variation of planetary boundary layer height (PBLH) in smoothed observationally derived dataset and MERRA2 reanalysis for June (left) and December (middle). The regions represented by each of the MERRA2 variations are shown in the right panel. Observationally derived PBLH is similar in magnitude and diel variation to MERRA2, which does not exhibit large spatial variation. In June, observationally derived profile is slightly lower than MERRA2 during midday.

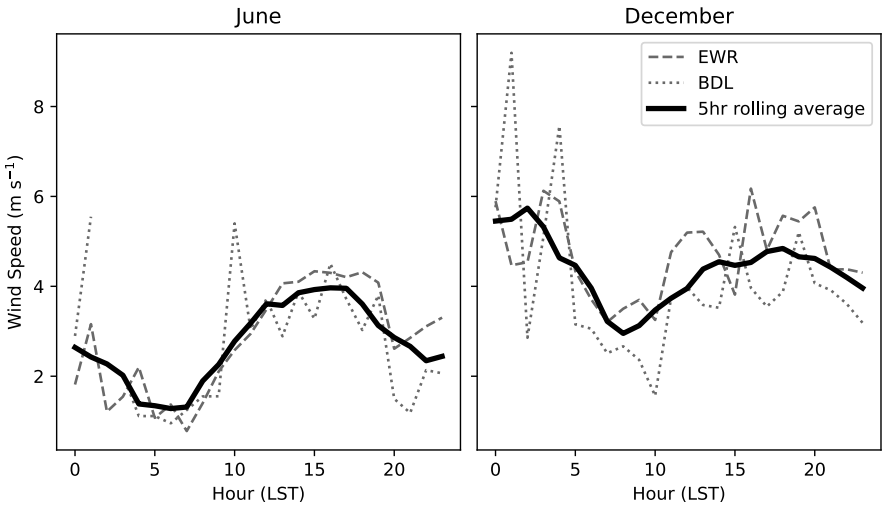

Figure S8. Comparison of average windspeed within the PBL from hourly data from Newark-Liberty International Airport (EWR) and Bradley International Airport (BDL) for June (left) and December (right) 2017. Average monthly windspeed for the box model (u) is defined as the five-hour centered rolling average of these data. Winds are notably higher in December than in June, which is consistent with seasonal shifts of synoptic-scale weather patterns in the northeastern US.

S2.2. Box model sensitivity to inclusion of chemical fluxes

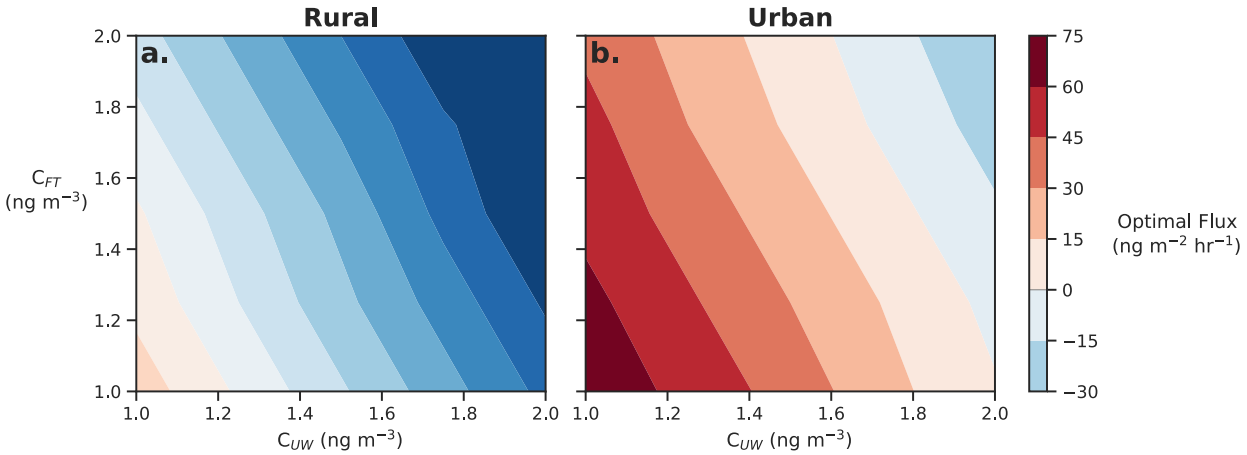

Figure S9. Solution space of the calibrated flux for combinations of C_{UW} and C_{FT} from 1 ng m^{-3} to 2 ng m^{-3} for (a) rural and (b) urban region in June 2017, including F_{Chem} implied by GEOS-Chem net chemical production of Hg^0.

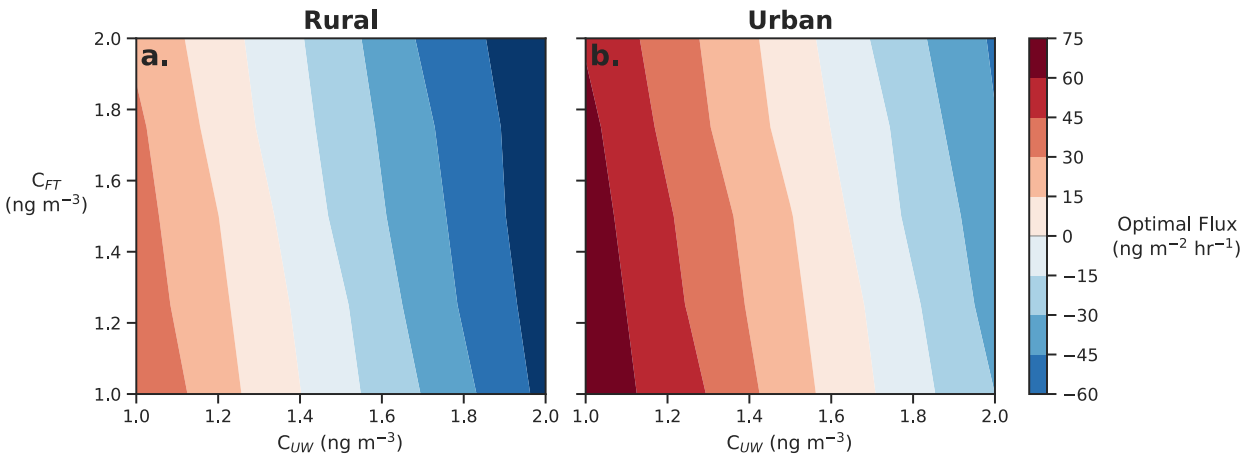

Figure S10. Solution space of the calibrated flux for combinations of C_{UW} and C_{FT} from 1 ng m^{-3} to 2 ng m^{-3} for (a) rural and (b) urban region in December 2017, including F_{Chem} implied by GEOS-Chem net chemical production of Hg^0.

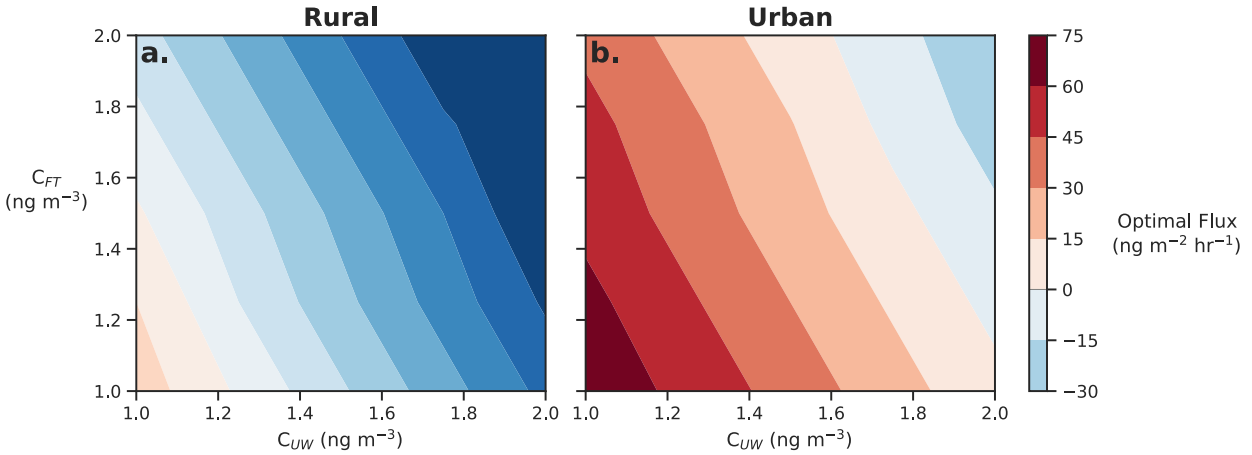

Figure S11. Solution space of the calibrated flux for combinations of C_{UW} and C_{FT} from 1 ng m^{-3} to 2 ng m^{-3} for (a) rural and (b) urban region in June 2017, including F_{Chem} implied by GEOS-Chem gross chemical loss of Hg^0.

S2.3. Box model quantitative sensitivity analysis

We evaluate the sensitivity of our calibrated fluxes to assumed diel profiles of horizontal windspeed (u) and planetary boundary layer height (z), along with the impact of the selected horizontal extent of the box (x) by rerunning the box model with these parameters adjusted by +/- 50% for June and December (tables S2 and S3, respectively). We evaluate box model sensitivity for values of C_{UW} and C_{FT} that correspond with values from the NEST, ANT7, and CFTSCAL sensitivity simulations for urban and rural regions. We specifically focus on these points to determine whether meteorological or model dimension parameter uncertainty is large enough to encompass the net regional fluxes simulated by the GEOS-Chem model. We specifically test three parameters in this analysis: u, x, and z. We indirectly evaluate the sensitivity of our box model to w_{PBL} when we scale z, as we calculate w_{PBL} as the time derivative of z.

Despite exhibiting sensitivity to meteorological and design-based parameters, we find that calibrated box model fluxes remain inconsistent with fluxes used to drive the GEOS-Chem model. The "model" columns of tables S2 and S3 contain the fluxes of the respective GEOS-Chem sensitivity simulation, and the corresponding calibrated box model flux. The remaining columns then show the calibrated flux obtained from the box model given a 50% increase or decrease in u, z (and by extension, w_{PBL}), and x. We find that increasing u and z leads to an increase in the calibrated flux magnitude, which is consistent with intuition since our flux calibration intends to match the average magnitude of observed concentrations in the rural or urban region, enhanced ventilation or dilution caused by u or z (and therefore w_{PBL}) would require a larger flux. Meanwhile, an increase in x results in a decrease in the calibrated flux, as the impact of ventilation is effectively dampened in the first term of equation 1. Critically, we find that the uncertainty induced by our box model assumptions is not large enough to affect our conclusion that GEOS-Chem surface fluxes are incompatible with current transport fluxes. Therefore, while meteorological uncertainties and model design choices can impact the quantitative characteristics and extent of flux solution spaces, these are insufficient to explain the fluxes employed by our GEOS-Chem simulations.

Table S2. Sensitivity of calibrated fluxes to box model parameters (June 2017)

June 2017		**Model**		**u**		**z/w_{pbl}**		**x**	
		GEOS-Chem	Box model	-50%	+50%	-50%	+50%	-50%	+50%
Rural	NEST	-2.6	6.3	3.8	8.9	3.8	11.4	11.4	6.4
	ANT7	-2.5	3.8	1.3	3.8	1.3	3.8	3.8	1.3
	CFTSCAL	-2.6	-16.5	-14.0	-21.6	-8.9	-26.7	-24.2	-14.0
Urban	NEST	1.4	47.0	31.8	57.2	24.2	69.9	69.9	36.9
	ANT7	16.4	34.3	24.2	41.9	16.5	49.6	49.6	29.2
	CFTSCAL	1.4	21.6	14.0	26.7	11.4	31.8	31.8	16.5

Table S3. Sensitivity of calibrated fluxes to box model parameters (December 2017)

Dec. 2017		Model		u		z/w_{pbl}		x	
		GEOS-Chem	Box model	-50%	+50%	-50%	+50%	-50%	+50%
Rural	NEST	0.5	1.3	1.3	3.8	1.3	3.8	3.8	1.3
	ANT7	0.85	-8.9	-3.8	-14.0	-3.8	-11.4	-16.5	-6.4
	CFTSCAL	0.5	-11.4	-6.4	-16.5	-6.4	-16.5	-21.6	-8.9
Urban	NEST	2.9	29.2	19.1	41.9	14.0	44.5	55.7	21.6
	ANT7	18.1	-1.3	1.3	-6.4	-1.3	-3.8	-8.9	1.3
	CFTSCAL	2.9	8.9	6.4	11.4	3.8	14.0	16.5	6.4

S2.4. Box model sensitivity to horizontal extent

To supplement the sensitivity analysis above, we evaluate the sensitivity of calibrated fluxes and the observationally constrained solution space to changes in horizontal extent (i.e., x) across the full range of C_{UW} and C_{FT} considered in the main text. Solution spaces for June 2017 with box model horizontal extent of 50 km and 200 km are shown in Figures S12 and S13, respectively. While the upper bound of horizontal extent considered here is larger than in table 2, we observe similar behavior, where a reduction in horizontal extent generally leads to an increase in calibrated flux, and an increase in horizontal extent leads to a decrease in calibrated flux. We also observe that the amplitude of concentrations simulated by the box model is sensitive to horizontal extent, with the optimal solution space encompassing a broader extent in the 200 km case than the 50 km case. Consistent with the sensitivity analysis in S2.2, we find that values of C_{UW}. C_{FT}, and net fluxes simulated by the GEOS-Chem model remain incompatible with these solution spaces, indicating that the findings of the main text are robust to conservative parameter uncertainty assumptions.

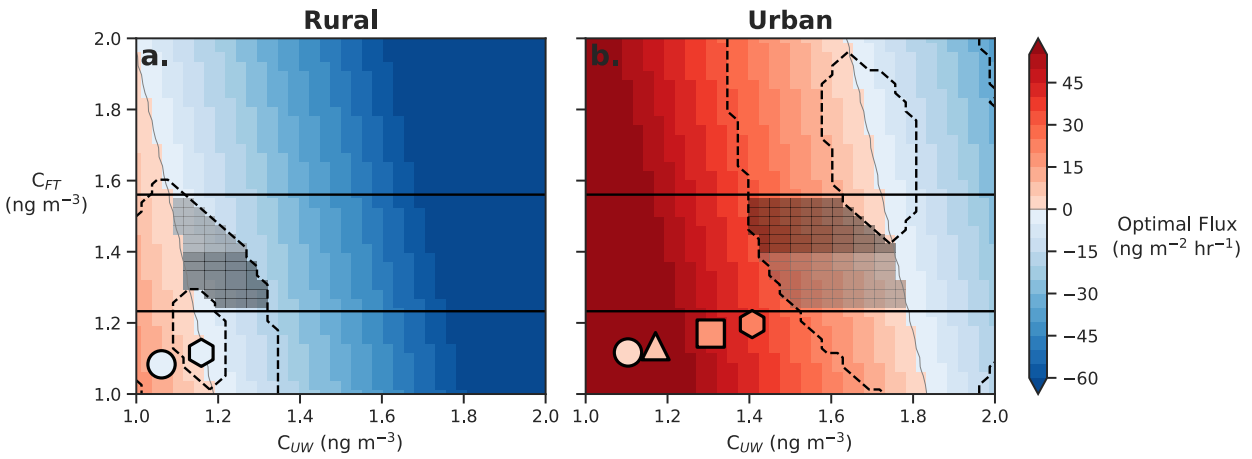

Figure S12. Solution space of the optimal flux for combinations of C_{UW} and C_{FT} from 1 ng m^{-3} to 2 ng m^{-3} for (a) rural and (b) urban regions, where the underlying box model has horizontal extent of 50 km. Horizontal solid lines refer to the likely bounds of C_{FT}, while dashed lines encompass the region of the space where simulated diurnal amplitude is within 50% of the observed value. Gray shading outlines the observationally constrained solution space, with the heavy shading indicating the region with highest confidence. GEOS-Chem simulation results are overlaid based on estimated values C_{FT} and C_{UW} and F for the respective region.

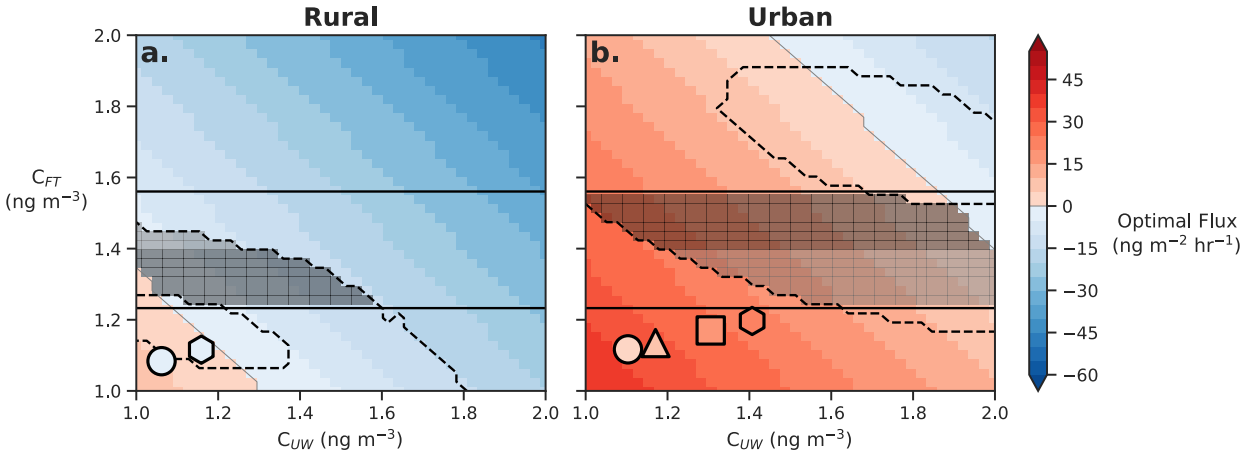

Figure S13. Solution space of the optimal flux for combinations of C_{UW} and C_{FT} from 1 ng m^{-3} to 2 ng m^{-3} for (a) rural and (b) urban regions, where the underlying box model has horizontal extent of 200 km. Horizontal solid lines refer to the likely bounds of C_{FT}, while dashed lines encompass the region of the space where simulated diurnal amplitude is within 50% of the observed value. Gray shading outlines the observationally constrained solution space, with the heavy shading indicating the region with highest confidence. GEOS-Chem simulation results are overlaid based on estimated values C_{FT} and C_{UW} and F for the respective region.

S2.5. Box model sensitivity to meteorological year

We evaluate the impact of interannual meteorological variability on the solution spaces presented in the main text. Box model results presented in the main text are driven using meteorological profiles from 2017 only, as we found that PBLH and wind speeds varied smoothly in both June and December, ensuring numerical stability of our box model. We decided not to average meteorology across years to avoid bias introduced by interannual variations in the quality and availability of measurements.

Diel profiles of PBLH and wind speed for June and December for each month averaged across Newark, NJ and Hartford, CT are plotted in Figures S14 and S15. PBLH reaches the highest daytime peak and lowest nighttime minimum in June 2017 of all the years considered. 2017 also has the highest daytime windspeed of all of the considered years, and has a moderate nighttime windspeed. While the magnitude of PBLH and windspeed can be important drivers of the behavior of the box model, their relative magnitude is important for the slope of contours within the solution space. We show that the variation for 2017 is relatively moderate. Unlike June, we observe that the diel profiles of PBLH, wind speed, and their ratios are moderate compared to other years in December.

To identify the potential bias introduced by this modeling choice, we repeat the analysis displayed in Figures 4 and 5 of the main text for 2012 (Figures S16 and S17) and 2018 (Figures S18 and S19). Consistent with the findings of the sensitivity analysis outlined above, the key GEOS-Chem sensitivity simulations remain outside of the observationally constrained solution space, and fluxes from the GEOS-Chem simulations generally do not correspond with the underlying solution spaces. Therefore, while we observe that the selected meteorological year can impact the quantitative distribution of calibrated fluxes, the key finding that GEOS-Chem regional surface fluxes and transport fluxes are incompatible with observations remains true.

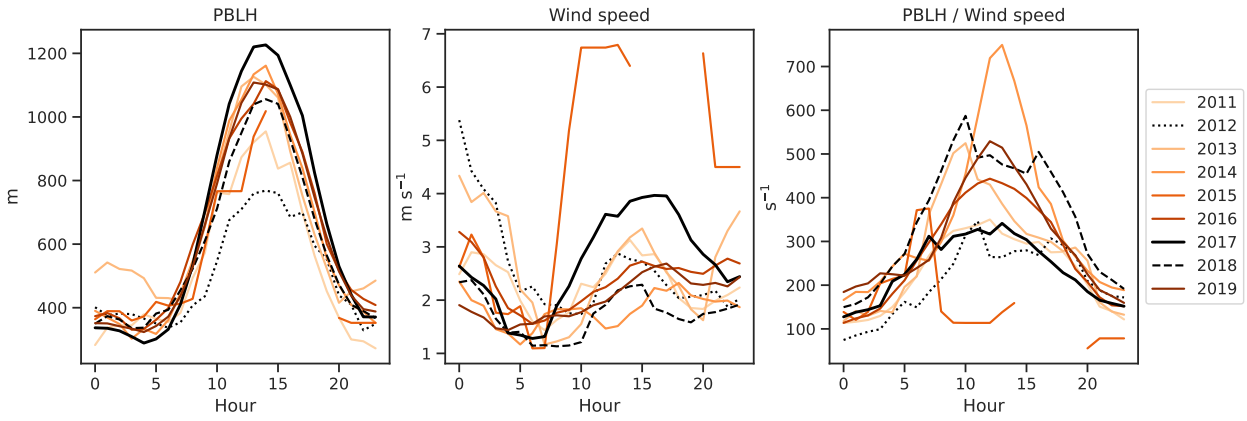

Figure S14. Comparison of June PBLH, Wind speed, and their ratio for 2011-2019 from aircraft-derived meteorological profiles (Zhang et al. 2020). 2015 data is especially impacted by limited observations, as evidenced by abnormal variations and afternoon data gaps.

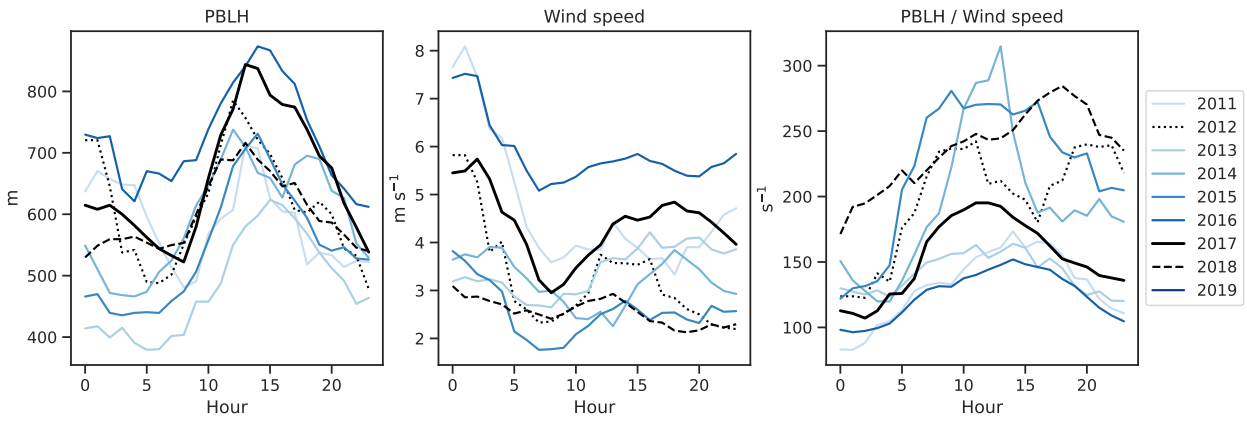

Figure S15. Comparison of December PBLH, Wind speed, and their ratio for 2011-2019 from aircraft-derived meteorological profiles (Zhang et al. 2020).

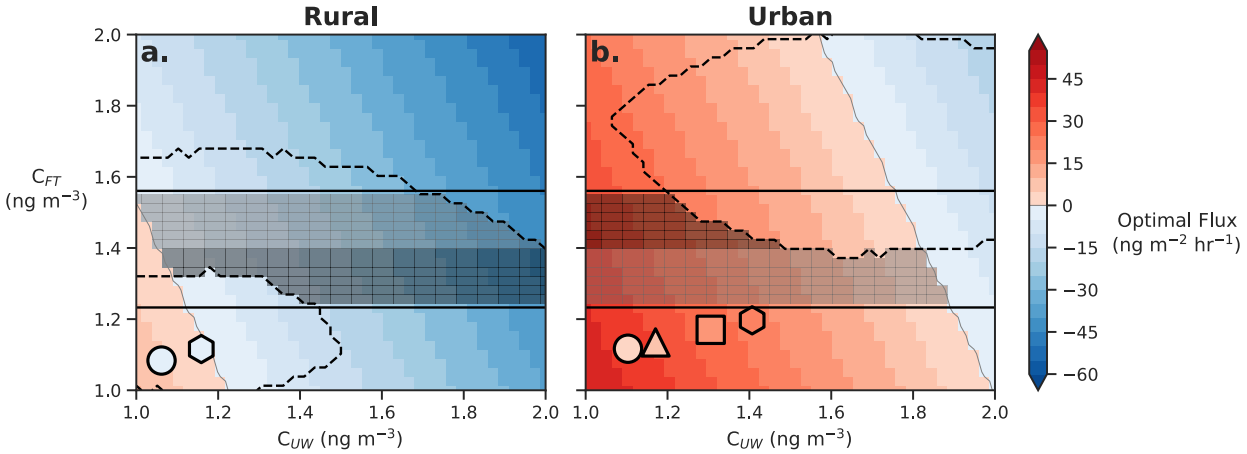

Figure S16. Solution space of the optimal flux for combinations of C_{UW} and C_{FT} from 1 ng m^{-3} to 2 ng m^{-3} for (a) rural and (b) urban regions using June 2012 meteorology. Horizontal solid lines refer to the likely bounds of C_{FT}, while dashed lines encompass the region of the space where simulated diurnal amplitude is within 50% of the observed value. Gray shading outlines the observationally constrained solution space, with the heavy shading indicating the region with highest confidence. GEOS-Chem simulation results are overlaid based on estimated values C_{FT} and C_{UW} and F for the respective region.

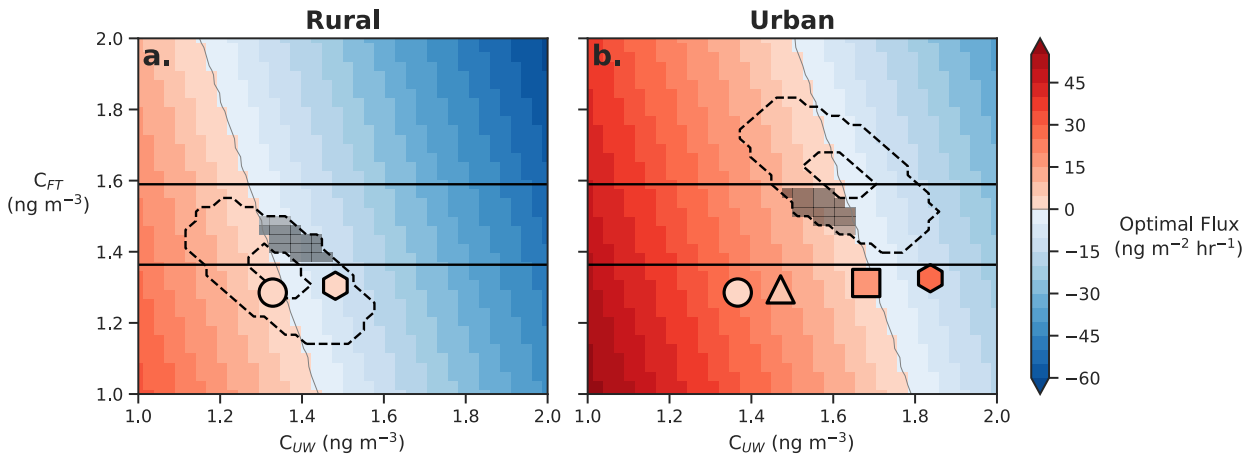

Figure S17. Solution space of the optimal flux for combinations of C_{UW} and C_{FT} from 1 ng m^{-3} to 2 ng m^{-3} for (a) rural and (b) urban regions using December 2012 meteorology. Horizontal solid lines refer to the likely bounds of C_{FT}, while dashed lines encompass the region of the space where simulated diurnal amplitude is within 50% of the observed value. Gray shading outlines the observationally constrained solution space, with the heavy shading indicating the region with highest confidence. GEOS-Chem simulation results are overlaid based on estimated values C_{FT} and C_{UW} and F for the respective region.

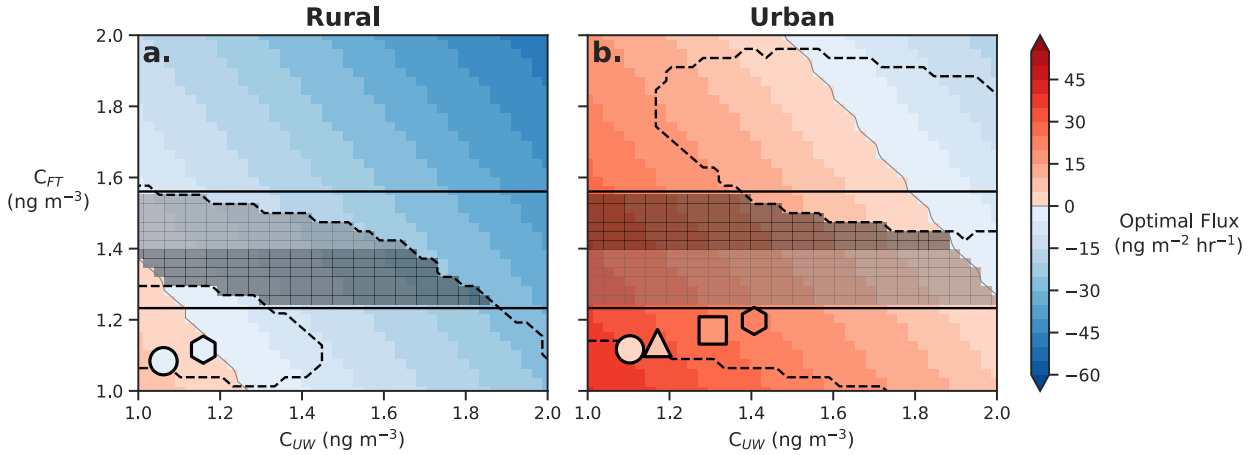

Figure S18. Solution space of the optimal flux for combinations of C_{UW} and C_{FT} from 1 ng m^{-3} to 2 ng m^{-3} for (a) rural and (b) urban regions using June 2018 meteorology. Horizontal solid lines refer to the likely bounds of C_{FT}, while dashed lines encompass the region of the space where simulated diurnal amplitude is within 50% of the observed value. Gray shading outlines the observationally constrained solution space, with the heavy shading indicating the region with highest confidence. GEOS-Chem simulation results are overlaid based on estimated values C_{FT} and C_{UW} and F for the respective region.

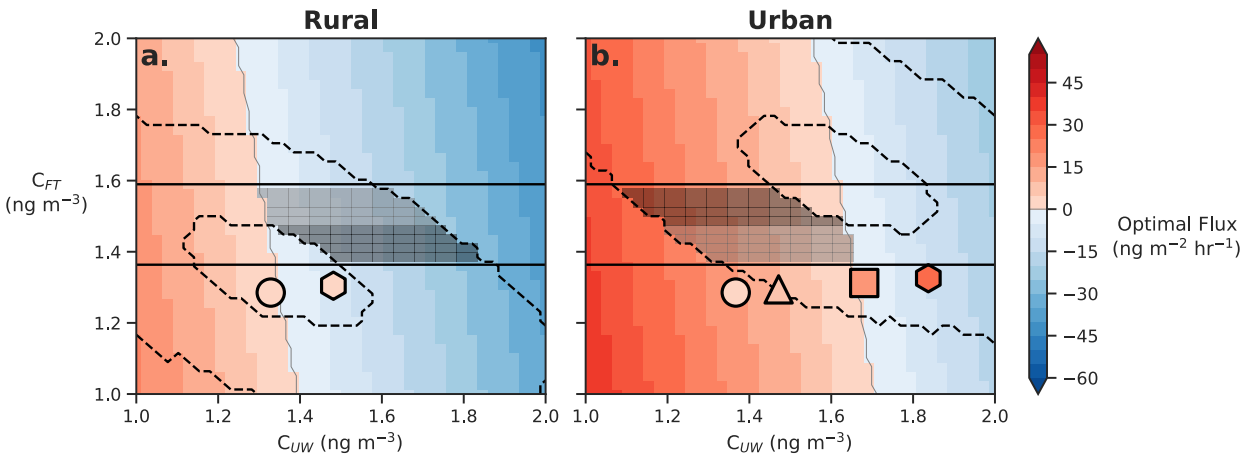

Figure S19. Solution space of the optimal flux for combinations of C_{UW} and C_{FT} from 1 ng m^{-3} to 2 ng m^{-3} for (a) rural and (b) urban regions using December 2018 meteorology. Horizontal solid lines refer to the likely bounds of C_{FT}, while dashed lines encompass the region of the space where simulated diurnal amplitude is within 50% of the observed value. Gray shading outlines the observationally constrained solution space, with the heavy shading indicating the region with highest confidence. GEOS-Chem simulation results are overlaid based on estimated values C_{FT} and C_{UW} and F for the respective region.

Section S2.6. Box model sensitivity to constant surface fluxes

Here, we demonstrate the negligible effect of allowing fluxes to vary temporally in our box model optimization to justify our use of constant fluxes in the main text. Over a limited number of combinations of C_{FT} and C_{UW}, we recalculate the optimal average flux in our box model when driven by a constant flux. Then, across the same domain, we repeat the same optimization while allowing the flux to vary in four hour segments. We find that average net fluxes are similar in both cases at both rural and urban sites (Figures S20, S22). We find that diurnally varying fluxes do reduce the difference between the observed diel variation when compared to the constant flux cases by reducing the extent of extremes (right panels, Figures S21 and S23). However, this is likely driven by overfitting, as we observe that this agreement is achieved unreasonably sharp temporal shifts in Hg fluxes that are not supported by any existing mechanisms (left panels, Figures S21 and S23). Furthermore, the diel average of these fluxes are similar in magnitude to the optimal fluxes obtained using constant values. The close correspondence of average fluxes from both methods, coupled with our overarching goal of finding the dominant drivers of diel variations in this region support our choice to drive our box model with temporally invariant surface fluxes in the main text.

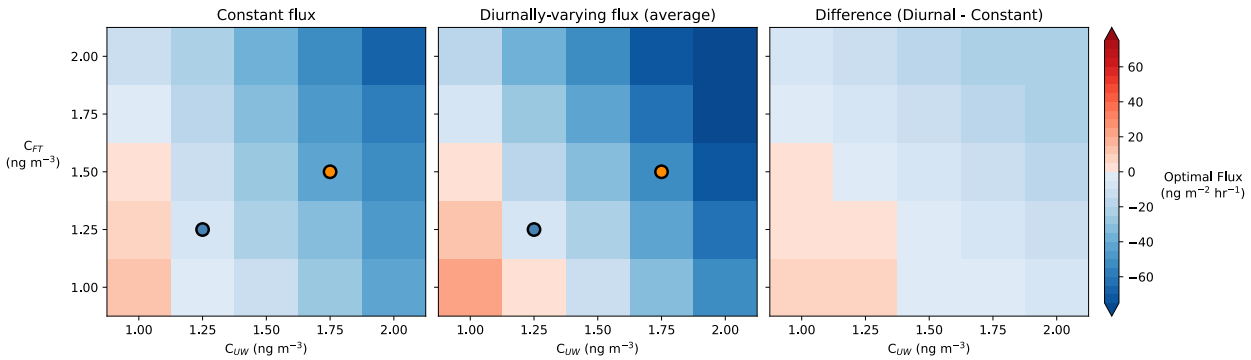

Figure S20. Comparison of optimal average surface flux at the rural sites predicted by box model with constant surface flux (left) or a diurnally-varying surface fluxes (middle), and their difference (right). Both approaches result in a qualitatively similar solution space, where the diurnally varying flux approach predicts larger average positive and negative fluxes. Blue and orange points represent concentration and flux combinations that are further explored in Figure S21.

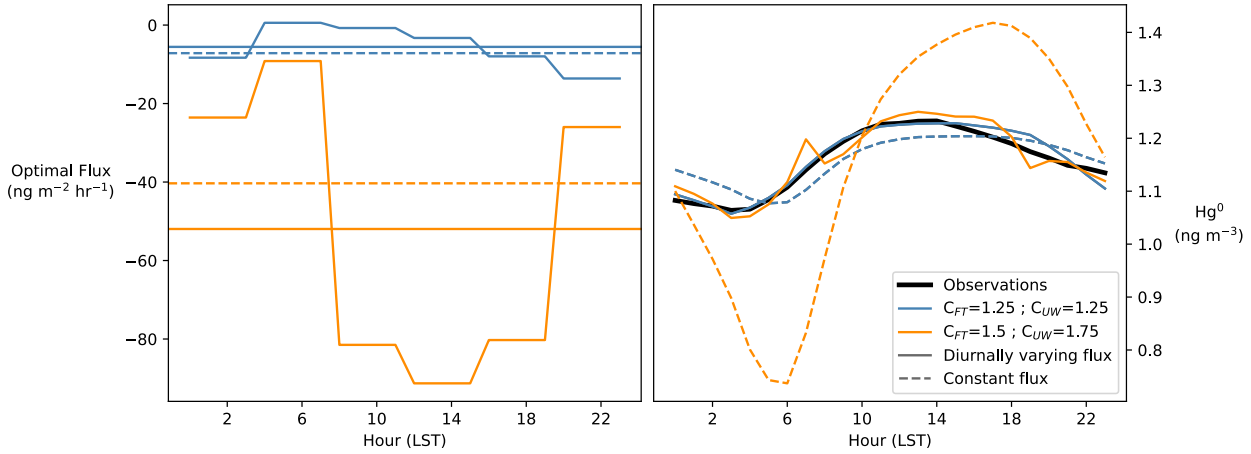

Figure S21. Comparison of the optimal constant flux and optimal diurnally varying flux for the two combinations of C_{FT} and C_{UW} shown in Figure S20 (left) and the respective variation of C_{PBL} (right). In both cases, the constant flux is similar in magnitude to the average of the temporally varying flux. The temporally varying flux simulates concentrations that lie closer to observations than the constant flux case.

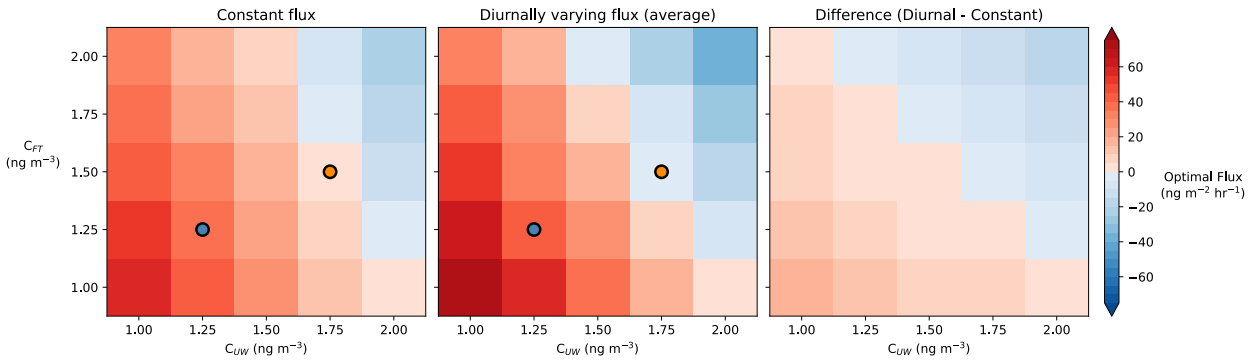

Figure S22. Comparison of optimal average surface flux at the urban sites predicted by box model with constant surface flux (left) or a diurnally-varying surface fluxes (middle), and their difference (right). Both approaches result in a qualitatively similar solution space, where the diurnally varying flux approach predicts larger average positive and negative fluxes. Blue and orange points represent concentration and flux combinations that are further explored in Figure S23.

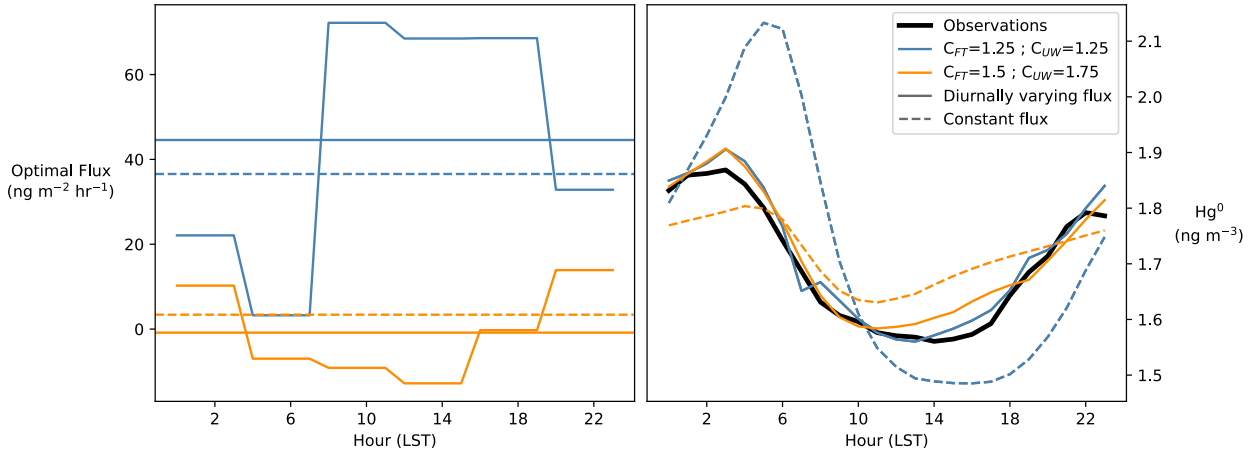

Figure S23: Comparison of the optimal constant flux and optimal diurnally varying flux for the two combinations of C_{FT} and C_{UW} shown in Figure S22 (left) and the respective variation of C_{PBL} (right). In both cases, the constant flux is similar in magnitude to the average of the temporally varying flux. Interestingly, for the case where C_{FT} = 1.5 (orange), the optimal fluxes from both methods have different signs on average, as the variable optimal predicts positive nighttime fluxes and negative daytime fluxes.

S3. GEOS-Chem Analysis

S3.1. List of GEOS-Chem simulations

Table S4. List of GEOS-Chem simulations used

Simulation	Resolution	Domain	Emission notes
STND	2°x2.5°	Global	GMA emissions
NEST	0.5°x0.625°	20°-70° N, 60°-100° W	GMA emissions
ANT3	0.5°x0.625°	20°-70° N, 60°-100° W	GMA scaled by factor of 3 (domain: 40°-50° N, 70°-80° W)
ANT7	0.5°x0.625°	20°-70° N, 60°-100° W	GMA scaled by factor of 7 (domain: 40°-50° N, 70°-80° W)
ANT10	0.5°x0.625°	20°-70° N, 60°-100° W	GMA scaled by factor of 10 (domain: 40°-50° N, 70°-80° W)
ANT3-ENA	0.5°x0.625°	20°-70° N, 60°-100° W	GMA scaled by factor of 3 across entire nested domain that covers eastern North America (see Fig. 1)
ANT7-ENA	0.5°x0.625°	20°-70° N, 60°-100° W	GMA scaled by factor of 7 across entire nested domain that covers eastern North America (see Fig. 1)
ANT10-ENA	0.5°x0.625°	20°-70° N, 60°-100° W	GMA scaled by factor of 10 across entire nested domain that covers eastern North America (see Fig. 1)
CFTSCAL	0.5°x0.625°	20°-70° N, 60°-100° W	GMA emissions, C_{FT} increased to approximately 1.4 ng m^{-3} by applying spatially and temporally uniform emission source of 5 x 10^{-15} kg m^{-2} s^{-1} at 3500 m above ground level
CFTSCALMAX	0.5°x0.625°	20°-70° N, 60°-100° W	GMA emissions, C_{FT} increased to approximately 1.8 ng m^{-3} by applying spatially and temporally uniform emission source of 1 x 10^{-14} kg m^{-2} s^{-1} at 3500 m above ground level
CFTSCAL-ANT7-ENA	0.5°x0.625°	20°-70° N, 60°-100° W	Includes adjustments from both the ANT7-ENA and the CFTSCAL sensitivity simulations.

S3.2. Relative contribution of chemical processing to Hg^0 fluxes within the PBL in GEOS-Chem

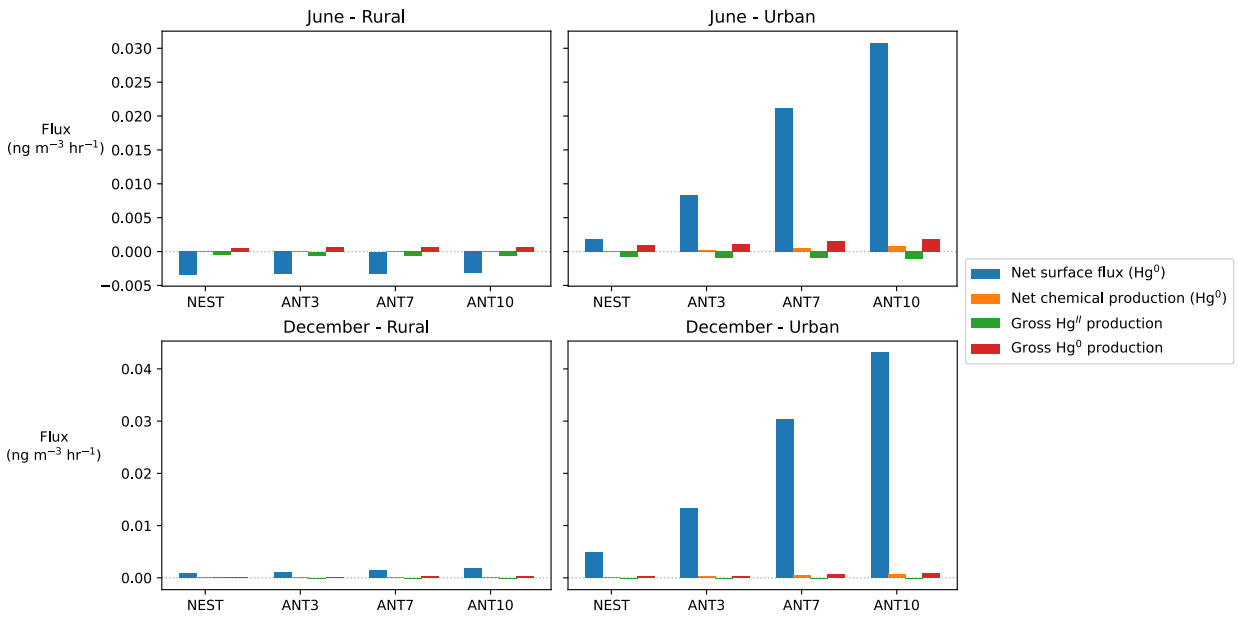

Figure S24. The relative magnitude of net surface fluxes and chemical fluxes within the planetary boundary layer in rural (left panels) and urban (right panels) regions, according to nested GEOS-Chem simulation in June (upper panels) and December (lower panels). Surface fluxes are normalized to represent their effect on average boundary layer concentrations by dividing by the average modeled PBLH for the respective month (see Fig S6). Regardless of the magnitude of anthropogenic emissions in this region, the magnitude of surface fluxes is 36-875 times larger than net chemical fluxes in the rural area and 21-30 times larger in the urban area.

S3.3. Estimating C_{FT} and C_{UW} from GEOS-Chem simulations

We describe our approach for estimating C_{FT} and C_{UW} from GEOS-Chem output below. We first define broad upwind domains for the rural and urban regions (green and orange boxes, left panel of Figures S25-S30). The broad horizontal extents of the upwind domains are selected to dampen the occasional effect of temporally varying winds that may occasionally pass through areas that are strong sources or sinks. Additionally, their locations are selected to be representative of the respective region, with mixed urban and suburban areas in New Jersey and Pennsylvania representing the upwind region for urban sites and upstate New York representing upwind region for rural sites. C_{UW} is calculated for each region as the average concentration within the upwind domains from the surface to the PBLH indicated by MERRA2 reanalysis. We define C_{FT} as the average hourly concentration of the column extending from the PBLH to 700 hPa above the midpoint between the measurement sites for respective regions (right panels of Figures S25-S30). The vertical extent of the PBLH exhibits hourly variation, however there is little difference in the average PBLH and its extent between urban and rural sites, supporting our use of spatially aggregated profiles for box model simulations described in Section 2.2 of the main text.

The NEST, ANT7, and CFTSCAL simulations in June show the impact of enhancing concentrations on spatial and vertical distribution. In the NEST simulation, concentrations throughout the domain are low and are highest over the ocean (Figure S25). Concentrations at urban centers including NYC and Boston do not notably deviate from lower concentrations in rural areas of the Northeastern US. A similar vertical distribution of Hg is observed at both urban and rural regions, with lower concentrations near the surface and higher concentrations aloft. In the ANT7 simulation, concentrations at urban centers are noticeably higher than in rural areas of the northeastern US, illustrating expected differences between known sink and source regions (Figure S26). This is also observed in vertical cross-section plots, where concentrations in the urban upwind domain are notably higher near the surface, while there is little impact in the rural areas. Notably, concentrations aloft are far less sensitive to regional emission enhancements than surface concentrations. In the CFTSCAL simulation, we find that direct enhancements to C_{FT} can effectively scale the surface features observed in the NEST simulation, with highest concentrations over the ocean and lower concentrations over land, consistent with the dominant influences of vegetative uptake fluxes and oceanic emissions in the model (Figure S27).

We also evaluate the vertical and horizontal distribution of Hg in the December sensitivity simulations (Figures S28-S30). Unlike June, there isn't a noticeable difference in Hg^0 concentrations between land and ocean in the NEST simulation (Figure S28). However, concentrations throughout the domain are notably higher in both horizontal and vertical dimensions in December, with highest concentrations in the southwestern portion of the domain (Figure S28). This is consistent with a lack of vegetative uptake in winter, resulting in a terrestrial shift from a summertime sink to wintertime source. We find that ANT7 results in large concentration enhancements near the surface that are more pronounced than in summer, which is likely driven by the combined influence of lower daytime PBLH and a lack of vegetative uptake to dampen this source (Figure S29). As in June, we find that the CFTSCAL simulation effectively enhances the existing spatial distribution of concentrations throughout the domain (Figure S30).

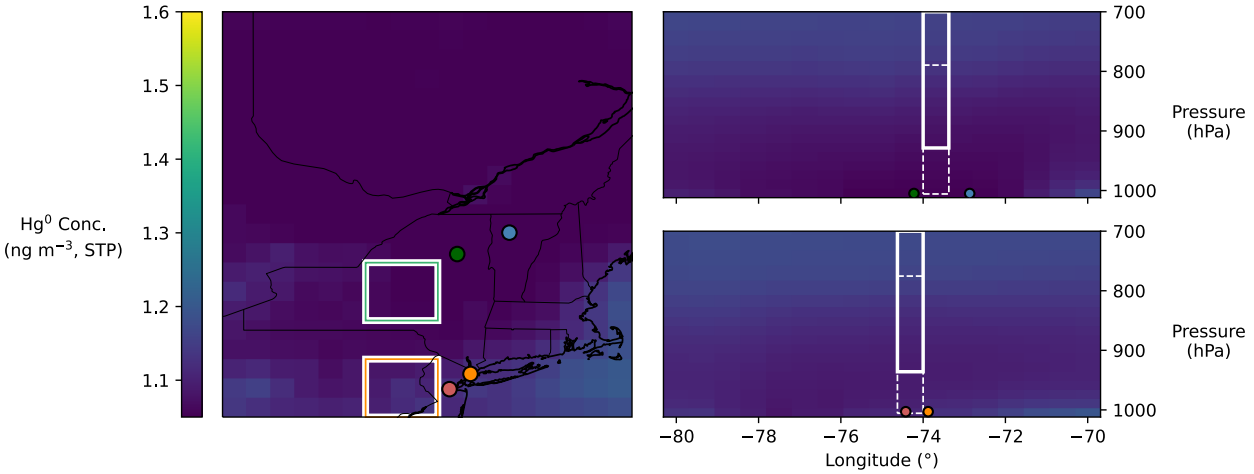

Figure S25. (left panel) Average surface concentration in June for the NEST simulation, where the green and orange boxes show the spatial region used to define C_{UW} for rural and urban sites, respectively. The upper and lower right panels show a horizontal cross section of the rural and urban latitudes to illustrate the average vertical distribution. The solid white boxes show the average height of the grid cells used to calculate C_{FT} in both regions, while the dashed lines show the range over which the lower bound of this region extends during the month.

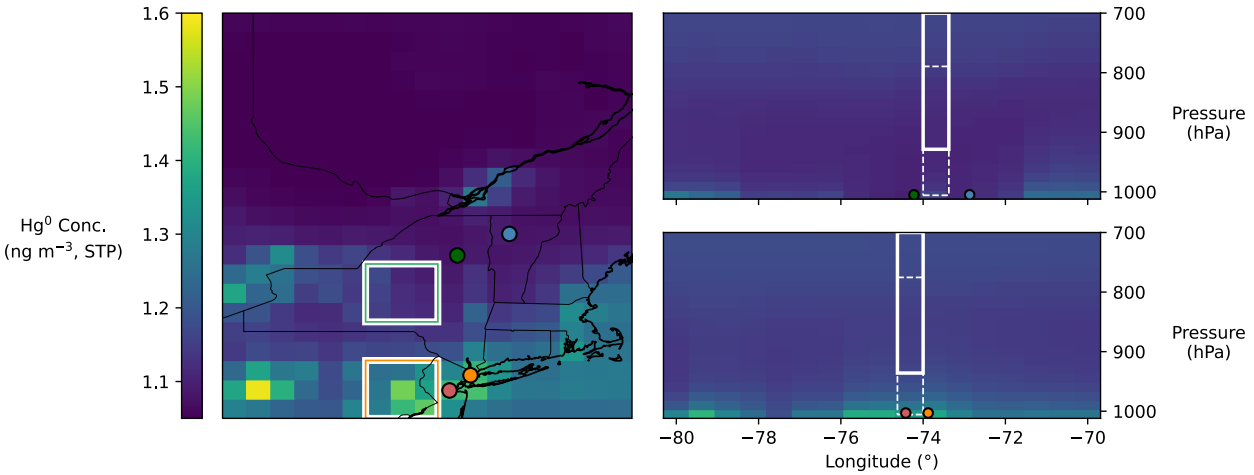

Figure S26. (left panel) Average surface concentration in June for ANT7 simulation, where the green and orange boxes show the spatial region used to define C_{UW} for rural and urban sites, respectively. The upper and lower right panels show a horizontal cross section of the rural and urban latitudes to illustrate the average vertical distribution. The solid white boxes show the average height of the grid cells used to calculate C_{FT} in both regions, while the dashed lines show the range over which the lower bound of this region extends during the month.

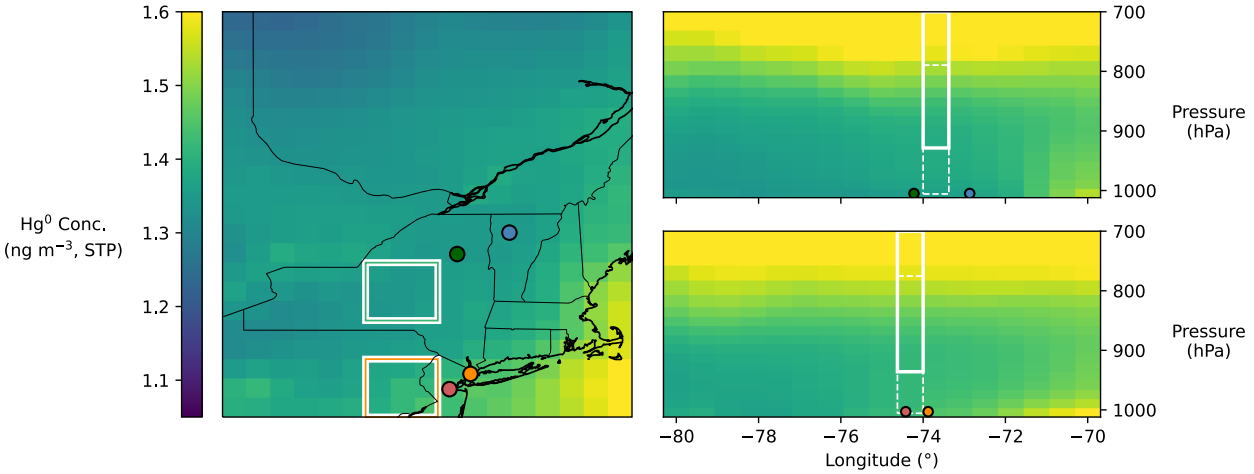

Figure S27. (left panel) Average surface concentration in June for the CFTSCAL simulation, where the green and orange boxes show the spatial region used to define C_{UW} for rural and urban sites, respectively. The upper and lower right panels show a horizontal cross section of the rural and urban latitudes to illustrate the average vertical distribution. The solid white boxes show the average height of the grid cells used to calculate C_{FT} in both regions, while the dashed lines show the range over which the lower bound of this region extends during the month.

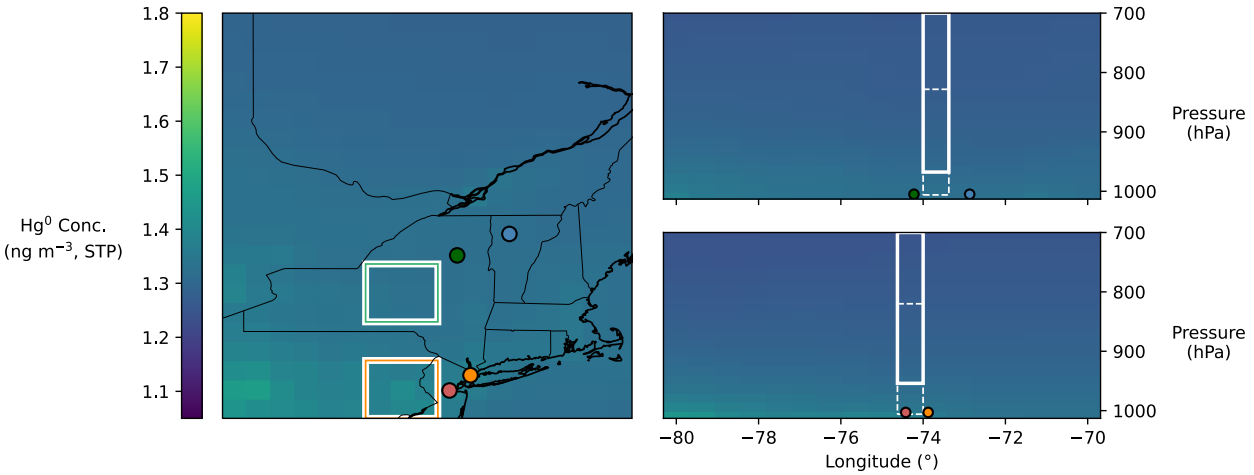

Figure S28. (left panel) Average surface concentration in December for the NEST simulation, where the green and orange boxes show the spatial region used to define C_{UW} for rural and urban sites, respectively. The upper and lower right panels show a horizontal cross section of the rural and urban latitudes to illustrate the average vertical distribution. The solid white boxes show the average height of the grid cells used to calculate C_{FT} in both regions, while the dashed lines show the range over which the lower bound of this region extends during the month.

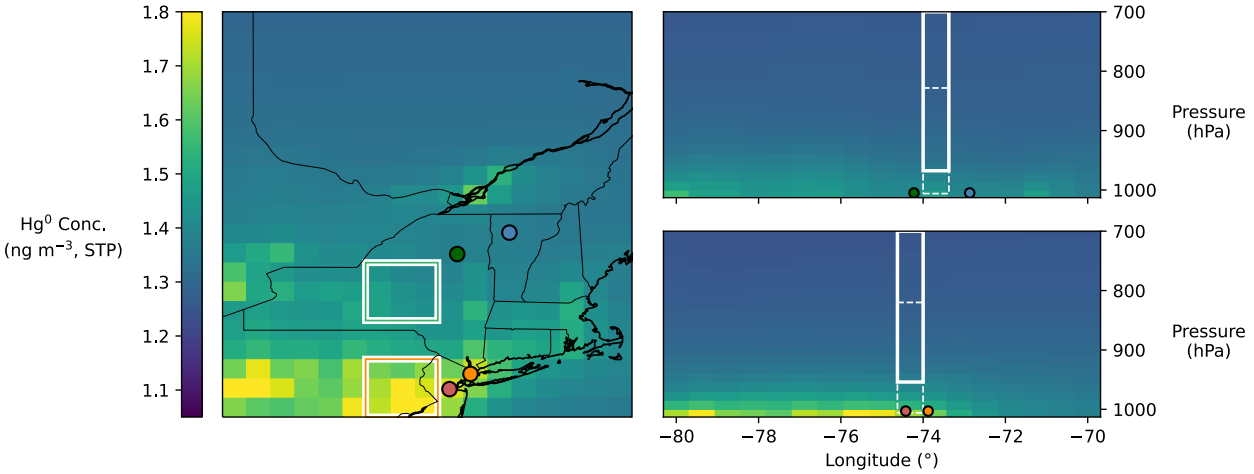

Figure S29: (left panel) Average surface concentration in December for the ANT7 simulation, where the green and orange boxes show the spatial region used to define C_{UW} for rural and urban sites, respectively. The upper and lower right panels show a horizontal cross section of the rural and urban latitudes to illustrate the average vertical distribution. The solid white boxes show the average height of the grid cells used to calculate C_{FT} in both regions, while the dashed lines show the range over which the lower bound of this region extends during the month.

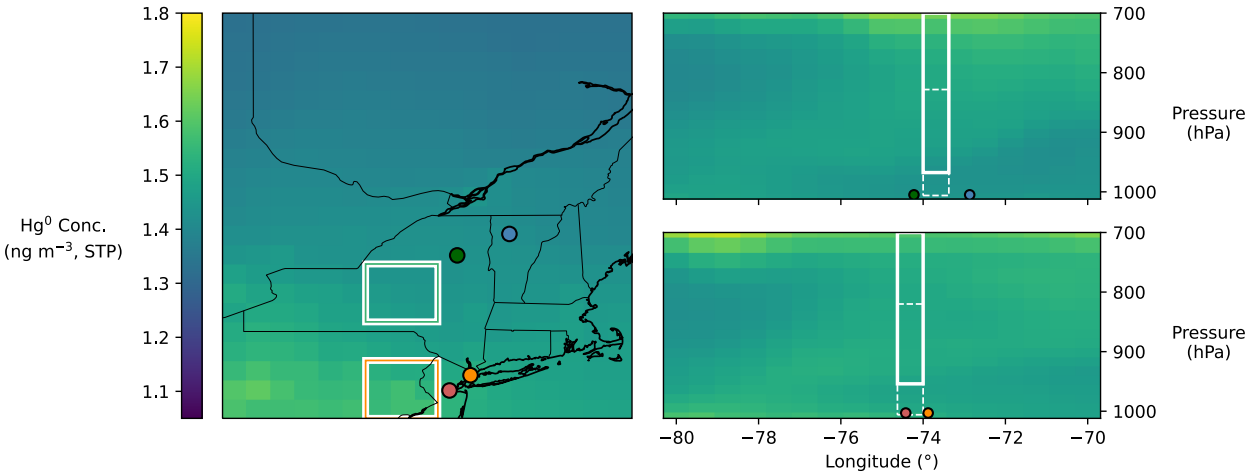

Figure S30: (left panel) Average surface concentration in December for the CFTSCAL simulation, where the green and orange boxes show the spatial region used to define C_{UW} for rural and urban sites, respectively. The upper and lower right panels show a horizontal cross section of the rural and urban latitudes to illustrate the average vertical distribution. The solid white boxes show the average height of the grid cells used to calculate C_{FT} in both regions, while the dashed lines show the range over which the lower bound of this region extends during the month.

Section S3.4. Impacts of anthropogenic emission scaling across eastern North America

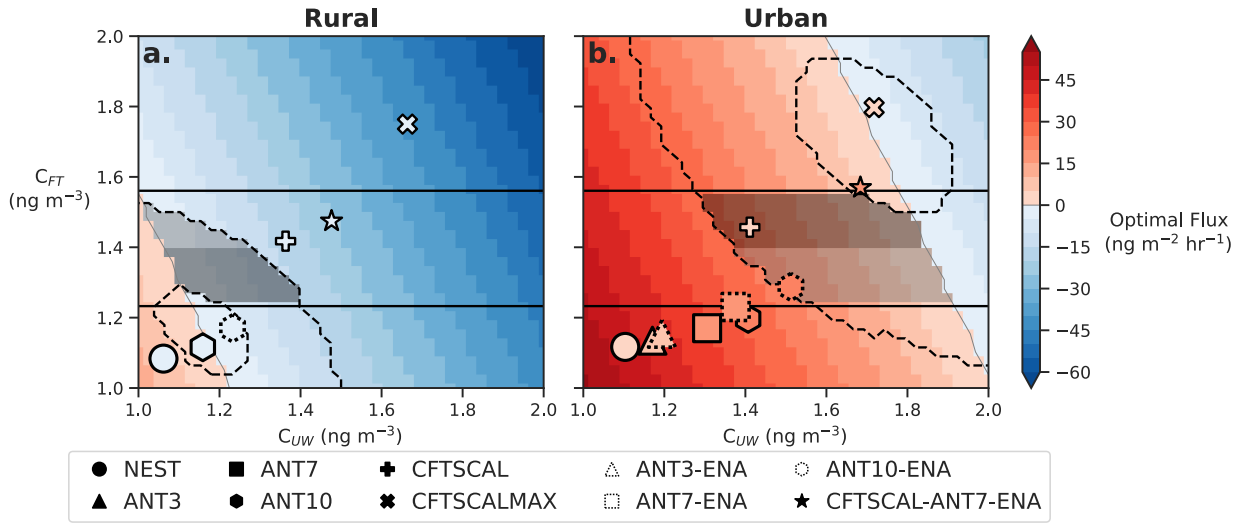

Figure S31. Same as Figure 4 of main text, here including results from the ANT3-ENA, ANT7-ENA, and ANT10-ENA sensitivity simulations as dashed outline boxes. By expanding the region over which emissions are scaled, C_{FT} and C_{UW} also increase, with the latter having more sensitivity.

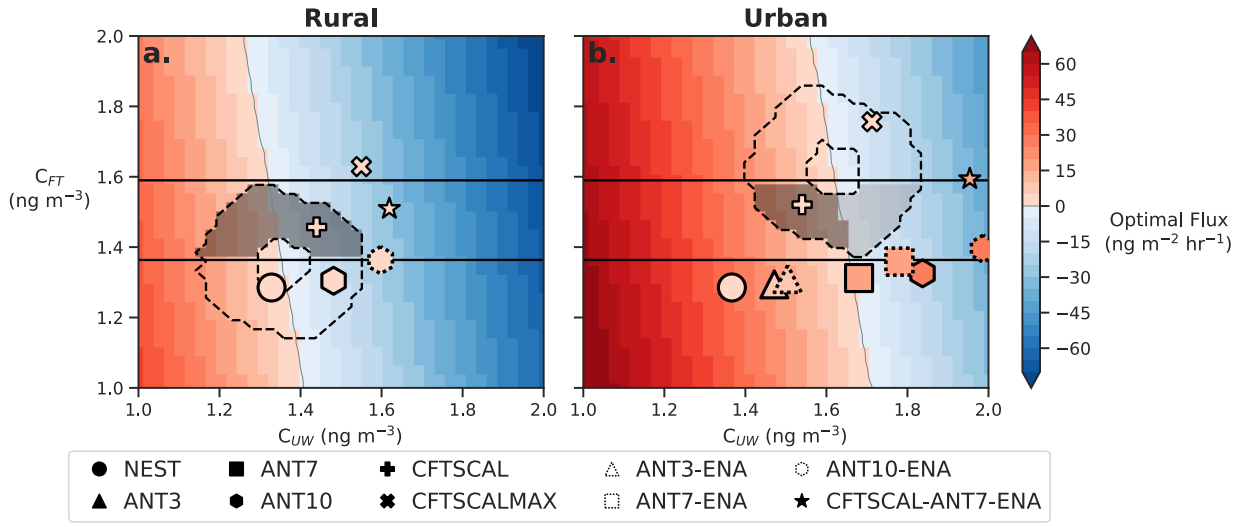

Figure S32. Same as Figure 5 of main text, here including results from the ANT3-ENA, ANT7-ENA, and ANT10-ENA sensitivity simulations as dashed outline boxes. By expanding the region over which emissions are scaled, C_{FT} and C_{UW} also increase, with the latter having more sensitivity.

Section S3.5. Further analysis of GEOS-Chem sensitivity simulations

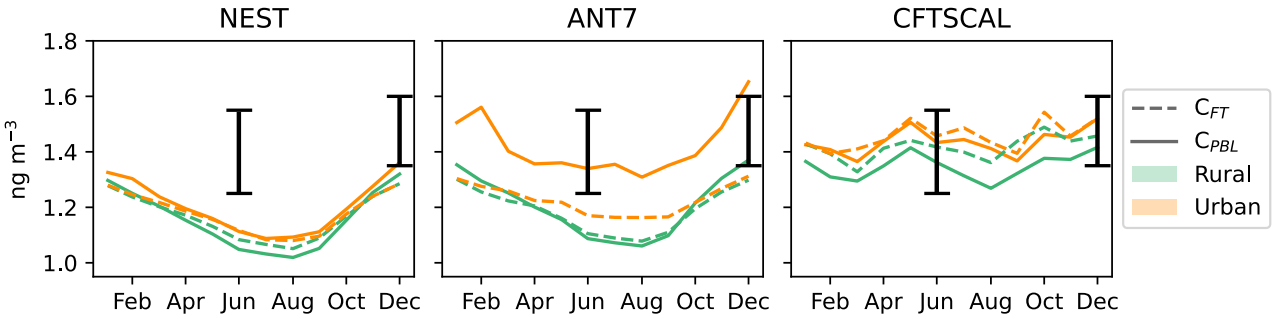

Figure S33: Seasonal variation of surface and free tropospheric concentrations (C_{PBL} and C_{FT}, respectively) at rural (green) and urban (orange) regions in NEST, ANT7, and CFTSCAL simulations. Black bars represent observational constraints on C_{FT} in June and December discussed in the main text. As previously discussed, NEST underestimates urban and rural C_{PBL} in June and December. ANT7 improves the expected spatial gradient of C_{PBL} but has limited impact on C_{FT}, which remains lower than observational constraints. Only the CFTSCAL simulation can satisfy observationally inferred constraints on C_{FT}, while also increasing the concentrations observed at the surface at these sites.